Synthesis of NiMo catalysts supported on Mn-Al2O3 for obtaining green diesel from waste soybean oil

I. Vázquez-Garrido, A. López-Benítez, Alfredo Guevara-Lara, G. Berhault

Synthesis of NiMo Catalysts supported on Mn-Al_2O_3 for obtaining Green Diesel from Waste Soybean Oil

I. Vázquez-Garrido[1], A. López-Benítez[1], A. Guevara-Lara[1,*], G. Berhault[2,*]

[1] Área Académica de Química, Universidad Autónoma del Estado de Hidalgo, Carr. Pachuca-Tulancingo Km. 4.5, C.P. 42184 Pachuca, Hidalgo, México.

[2] Institut de Recherches sur la Catalyse et l'Environnement de Lyon, CNRS – Université Lyon I, 02 avenue Albert Einstein, 69100 Villeurbanne, France

All correspondence should be sent to:

Alfredo Guevara-Lara:

Ph: (+52) 7717172000 ext 2202. Fax: (+52) 7717172000 ext 6502

E-mail: guevaraa@uaeh.edu.mx

Or to:

Gilles Berhault

Ph: (+33) 472 44 53 07

Fax: (+33) 472 44 53 99

E-mail: gilles.berhault@ircelyon.univ-lyon1.fr

Abstract

The influence of adding manganese to an Al_2O_3 support for preparing NiMo catalysts for the hydroconversion of soybean oil was herein evaluated. Two different Mn contents (1 and 5 mol % Mn) were used while Al_2O_3-Mn_x (x = 1 or 5 % mol Mn) were obtained by sol-gel method. The NiMo catalysts were obtained by wetness co-impregnation of nickel and molybdenum precursors onto the as-formed supports considering two different pH of impregnation (5 or 9). Solids were then characterized at the oxide state at different stages of preparation before being sulfide at 400°C for 4 h with 10% H_2S/H_2. Catalysts were then characterized at the sulfide state and evaluated for the hydroconversion of new and waste soybean oil at 380°C, P_{H2} = 40 bars. Results show clearly the superiority of NiMo catalysts supported on Al_2O_3 with 1% mol Mn for the hydroconversion of new and waste soybean oil due to the stabilization of manganese oxide species on the alumina support helping to redisperse the Ni-promoted MoS_2 active phase. This study shows that through a precise control of the addition of manganese to Al_2O_3, it is possible to obtain very highly active NiMo catalysts for the hydroconversion of vegetable oils.

Keywords

NiMo; Hydrodeoxygenation; Manganese; Soybean Oil; Green Diesel

1. Introduction

Transesterification of triglycerides with methanol is the standard way to produce biodiesel. However, this reaction presents several disadvantages including the formation of large amount of glycerol as by-product [1]. The main products of the transesterification reaction, methyl esters of fatty acids, are oxygenated compounds presenting a cetane index unsuitable for direct use in diesel engines [2, 3]. Moreover, the transesterification yield decreases when using waste vegetal oil [4]. Waste oils are residues of the food industry presenting high humidity and acidity indexes [4].

Catalytic hydroconversion is able to transform fatty acids into linear chain alkanes with characteristics similar to commercial diesel but with better cetane index and better cold flow properties [4]. Catalytic hydroconversion can be performed in a hydrotreating unit with an heterogeneous catalyst (generally NiMo, CoMo, or NiW hydrotreating catalysts), high temperatures (320-410°C) and high hydrogen pressures (30 to 80 bars) [5, 6]. The reaction mechanism occurring during the catalytic hydroconversion of triglycerides is shown in Figure 1. The first step is the hydrogenation of the C=C bonds of triglycerides followed by a C-O hydrogenolysis reaction leading to the formation of three moles of fatty acids and one mole of propane [1]. In a second step, oxygen atoms from fatty acid molecules are removed in order to form liner chain hydrocarbons through a deoxygenation reaction. Fatty acid deoxygenation can occur through three main mechanisms. Hydrodeoxygenation (HDO) leads to octadecane, hexadecane and water. On the contrary, heptadecane, pentadecane, CO and CO_2 are formed through decarboxylation (DCO_2) and decarbonylation (DCO) [5-12].

Catalytic hydroconversion can be performed using sunflower [1], soybean [13], palm [14], colza [15] or jatropha [16] oils with commercial $NiMo/Al_2O_3$ catalysts in order to generate green diesel. Catalysts based on noble metals like Pd/C [17], Pt/C [18], Pt/Al_2O_3 [19], Pt/Zeolite [20] and Pd/SiO_2 [21] present better selectivity along the DCO and DCO_2 pathways with a minor hydrogen consumption than NiMo catalysts. However, in this case, a lower cetane index is obtained due to the formation mainly of heptadecane and pentadecane. Moreover, Pd/C catalysts strongly deactivate in the presence of high fatty acid concentrations [17] while Pt/C, Pd/SiO_2 and Pt/zeolite catalysts exhibit a high hydrocracking activity unsuitable for green diesel production [18, 20, 21]. Nickel catalysts have also been envisaged since more cost effective than noble metals. In this respect, Liu et al. [22] have used Ni and NiAg catalysts supported on zeolites for the conversion of castor oil. Ni/C [23], Ni supported on carbon nanotubes [24], Ni/Al_2O_3 and Ni/SiO_2 [25] catalysts have also been studied with encouraging results.

Nickel phosphides supported on zeolites have also been investigated for biodiesel production [26]. Ren et al. [27] also studied molybdenum carbide for propanal deoxygenation. They observed a higher propensity for C-O than for C-C bond hydrogenolysis. However, these latter catalysts can suffer from sintering while being more costly and with a lower activity compared to promoted molybdenum sulfides.

MoS_2 catalysts promoted by nickel have been used in a large extent for hydroconversion applications due to their high intrinsic activity [1, 5-12, 14-16]. Their interesting catalytic properties are related to the presence of the so-called promoted NiMoS phase. This active phase is generally described as being formed of more or less stacked MoS_2 slabs with promoting atoms located at the edges of molybdenum sulfide layers [28-36]. Active sites on the NiMoS phase are generally recognized to be coordinatively unsaturated sites (or CUS) localized at the edges of Ni-promoted MoS_2 slabs [37, 38]. In this respect, Veriansyah et al. [39] demonstrated the interest of using the Al_2O_3-supported NiMo catalysts by comparison to different other alumina-supported systems for the hydrotreatment of soybean oil. They observed that the activity of the different catalysts decreases in the following order: NiMo (92.9%) > Pd (91.9%) > CoMo (78.9%) > Ni (60.8%) > Pt (50.8 %) > Ru (39.7%). They also found that the final composition of the biodiesel was directly related to the type of catalysts used. Biodiesels obtained using Pd, Ni, Pt and Ru present a higher proportion in heptadecane while the use of NiMo leads to a high activity along the HDO pathway. The high deoxygenation efficiency as well as the low cost of NiMo and CoMo catalysts would then make particularly suitable for triglyceride hydroconversion.

The nature of the promoter atom used in combination with MoS_2 catalysts has been also evaluated. Kim et al. [8] studied the differences in distribution products when using Co or Ni as promoter of MoS_2 catalytic systems. The NiMo catalyst leads to a lower content of alkenes while using CoMo results in a higher amount of isoalkanes. They therefore concluded that the biodiesel obtained using the NiMo catalyst has better properties under cold flow conditions. Zhang et al. [9] studied the effect of the promoter for the hydroconversion of vegetable oils using bulk molybdenum sulfide catalysts in order to disregard any interfering effect coming from the support. The Ni promotion led to a higher selectivity along the HDO pathway while the Co promoter favored the DCO and DCO_2 pathway. They ascribed these differences to a higher propensity of NiMo catalysts to form CUS active sites. Moreover, Toba et al. [40] emphasized the fact that the CoMo catalytic system exhibits a lower resistance to deactivation than NiMo due to the formation of water during the reaction. This work is in agreement with a

study made by Senol et al. [41] showing that the addition of water engenders a higher deactivation of CoMo catalysts than of NiMo even if a sulfiding agent is present.

In catalytic hydroconversion reactions, the nature of the support plays an important role towards activity and selectivity. Different types of supports have then been studied like zeolites, silica, alumina, or titania. In this respect, Mikulec et al. [12] studied the influence of the support using NiW and NiMo catalysts. They found a relationship between the variation of the C17/C18 ratio and the nature of the support. The tendency to decarboxylation/decarbonylation decreases in the following order: NiW/NaY > NiW/TiO_2 > NiMo/TiO_2 > NiW/ZrO_2 > NiMo/Al_2O_3 showing a correlation with the acidity of the support. This latter parameter also influences the degree of hydrocracking and isomerization. Qian et al. [42] synthesized NiMo catalysts supported on bifunctional zeolites and found higher hydrocracking and isomerizing activities than for NiMo/Al_2O_3 due to the enhanced Brönsted acidity associated with the use of zeolites. Coumans et al. [43] investigated the effect of different supports (carbon, SiO_2, amorphous silica-alumina and Al_2O_3) on the catalytic activity of NiMo systems for the hydrodeoxygenation of methyl oleate used as a representative molecule of the transformation of triglycerides into green diesel. They observed the following tendency for the initial rate of hydrodeoxygenation: NiMo/ Al_2O_3 > NiMo/ASA > NiMo/C > NiMo/SiO_2. Moreover, they found that the nature of the support also influences significantly the morphology of the active phase (dispersion and stacking of the MoS_2 slabs). The NiMo/Al_2O_3 catalyst presents a lower initial stacking than the other catalysts. However, after 7 days of reaction, the NiMo/C catalyst showed the highest activity. This effect was attributed to a better dispersion associated with a minor stacking of the MoS_2 slabs promoted by Ni.

In the same way, the addition of manganese can enhance the hydrodesulfurization activity of NiMo/Al_2O_3 thanks to a better dispersion of the NiMoS active phase. In this respect, López-Benítez et al [44] demonstrated that the addition of 1% mol of Mn (as MnO) to the alumina support increases significantly the hydrodesulfurization of dibenzothiophene.

Based on these previous findings, the objective of this study will be to characterize NiMo catalysts supported on Mn-Al_2O_3 mixed oxide at the sulfide state and to evaluate their catalytic performance for the hydroconversion of new and waste soybean oil.

2. Experimental

2.1. Synthesis of the supports

The Al_2O_3 support used as reference was prepared by a sol-gel method. First, aluminum isopropoxide ($Al(OC_3H_7)_3$) was first dissolved in 1-propanol (1 g alkoxide/10 ml alcohol). The gel was obtained through hydrolysis by addition of deionized water dropwise. The gel was then dried at 120°C for 12 h and then calcined at 500°C (5°C/min) for 4 h.

The Mn-Al_2O_3 supports were prepared by the sol-gel method developed by López-Benítez et al [44]. Aluminum isopropoxide and manganese acetate ($Mn(C_2H_3O_2)_2$) were dissolved separately in 1-propanol (1 g alkoxide/10 ml alcohol). After homogeneization, the two solutions were mixed. The gel was obtained through hydrolysis by addition of deionized water dropwise. The solid was then dried at 120°C for 12 h and calcined at 500°C (5°C/min) for 4 h. The supports with 1 and 5% mol Mn (as MnO) were called Al_2O_3-Mn_1 and Al_2O_3-Mn_5, respectively.

2.2. Synthesis of catalysts

Catalysts were prepared by wetness co-impregnation with 14 wt % MoO_3 loading and using a Ni/(Ni + Mo) molar ratio of 0.3. Two impregnation solutions were prepared by dissolving nickel nitrate hexahydrate ($Ni(NO_3)_2 \cdot 6H_2O$) and ammonium heptamolybdate tetrahydrate ($(NH_4)_6Mo_7O_{24} \cdot 4H_2O$) in 1) deionized water at pH = 5 and 2) in an NH_4OH aqueous solution adjusted at pH = 9. After impregnation, the catalysts were dried at 120°C for 12 h before being calcined at 400°C for 4 h. The catalysts prepared at pH = 5 were called NiMo/Al_2O_3-pH5, NiMo/Al_2O_3-Mn_1-pH5 and NiMo/Al_2O_3-Mn_5-pH5. The catalysts impregnated with the solution at pH = 9 were called NiMo/Al_2O_3-pH9, NiMo/Al_2O_3-Mn_1-pH9 and NiMo/Al_2O_3-Mn_5-pH9. Finally, catalysts were sulfided at 400°C (5°C/min) for 4 h using a 10 % (v/v) H_2S in H_2 mixture (4L/h).

2.3. Support characterization

The supports were characterized by ζ-potential and N_2 physisorption measurements. Zeta potential measurements were performed using a Malvern ZetaSizer Nano ZS90 equipment. 0.02 g of each support was dispersed in 200 mL of a $NaNO_3$ 0.01 M electrolyte solution at 25°C. The pH was adjusted with aqueous solutions of 0.1 M NH_4OH and 0.1 M HNO_3.

N_2 physisorption measurements were performed using an ASAP 2020 Micromeritics apparatus. Before measurement, the samples were treated at 300°C for 4 h down to P = 30 x 10^{-5} mm Hg. The specific surface areas and pore sizes were calculated applying the Brunauer-Emmett-Teller (BET) and Barrett-Joyner-Halenda (NJH) models respectively.

2.4. Catalyst characterization at the oxide state.

The catalysts at the oxide state have been characterized by UV-vis diffuse reflectance (UV-Vis DRS) and Raman spectroscopies. The UV-vis DR spectra were obtained using a Perkin-Elmer Lambda 35 spectrophotometer equipped with an integration sphere. Spectralon SRS-99-010 (99% of reflectance) was used as standard. The data obtained were treated using the Kubelka-Munk function:

$$F(R\infty) = \frac{(1-R\infty)^2}{2R\infty} \quad (1)$$

where $R\infty$ is the reflectance at infinite depth.

The Raman spectra were obtained with a Raman BWTEK-iplus spectrometer equipped with a 20, 50 and 100 x microscope, a 532 nm laser and a HQE-CCD detector. An accumulation of 10 scans was obtained for each sample. The laser intensity was limited to 50 mW to avoid any damage of the samples.

2.5. Catalyst characterization at the sulfide state.

The catalysts at the sulfide state were characterized by inductively coupled plasma optical emission spectroscopy (ICP-OES), X-ray photoelectron spectroscopy (XPS), high resolution transmission electron microscopy (HRTEM) and pyridine adsorption followed by infrared spectroscopy.

The amounts of Ni, Mo, and Mn were determined by ICP-OES analysis using a Horiba Jobin Yvon Activa spectrometer. Before analysis, the samples were treated with a H_2SO_4-HNO_3-HF mixture (1:1:0.5 v/v/v ratio) followed by maximum evaporation.

The XPS study was performed on an Axis Ultra DLD (Kratos analytical) spectrometer with an Al Kα radiation (1486.6 eV). The catalysts at the sulfide state were manipulated under argon atmosphere (without air contact) and were placed on a sample holder covered with indium foil.

The binding energies were fixed according to the adventitious C 1s level at 284.6 eV. Mo 3d and Ni 2p spectra were decomposed using mixed Gaussian-Lorentzian functions after a Shirley-type baseline subtraction treatment (CasaXPS software, version 2.0.71) [45, 46].

The atomic percentages [i] were determined considering the total area of the Ai corresponding peak and using a sensitive factor Si:

$$[i] = \frac{\frac{A_i}{S_i}}{\sum_{i=1}^{n}(\frac{A_i}{S_i})} \quad (2)$$

The Mo 3d and Ni 2p core level spectra can be decomposed into three contributions corresponding to MoS_2, MoO_xS_y and MoO_3 for Mo and to NiS_x, NiMoS, and NiO_x for Ni [47, 48]. The proportion of NiMoS phase was determined as follows:

$$\%NiMoS = \frac{A_{NiMoS}}{A_{NiMoS} + A_{NiOx} + A_{NiSx}} x\ 100 \quad (3)$$

where A_{NiMoS} , A_{NiOx} y A_{NiSx} correspond respectively to the NiMoS, NiO_x and NiS_x species.

HRTEM images were acquired using a JEOL 2010 (200 kV) microscope. Sulfided catalysts were first dispersed ultrasonically in ethanol. The suspension was then deposited onto a C-covered Cu grid. Molybdenum sulfide based catalysts present a layered structure with particles forming stacked slabs. Statistical analyses were performed considering 10 different micrographs (5170 nm^2 for each micrograph) coming from various regions of the studied samples (600-800 counted particles). The average stacking number and the average slab length were obtained using the following equations [49]:

$$\overline{N} = \frac{\sum_{i=1}^{n} n_i N_i}{\sum_{i=1}^{n} n_i} \quad (4)$$

$$\overline{L} = \frac{\sum_{i=1}^{n} n_i l_i}{\sum_{i=1}^{n} n_i} \quad (5)$$

with N_i and l_i representing the stacking number and the MoS_2 slab length directly determined from TEM images, n is the number of particles measured in a size interval or the stacking number of index i.

The acid properties of the sulfided catalysts were analyzed by lutidine (2,6-dimethylpyridine) adsorption followed by infrared spectroscopy following the methodology reported by Berhault et al. [50, 51], varying the adsorption temperature at constant concentration in lutidine. The infrared spectra were obtained with a Perkin-Elmer FTIR spectrophotometer. Disks were prepared with a 15% wt/wt mixture of the catalyst in inert alumina. Samples were pressed in disks of 0.6 cm radius, with a 5.10^{-3} cm thickness and a 17 mg weight. Disks were then placed

on a sample holder inside a tubular cell equipped with calcium fluoride (CaF_2) windows. The disks were then in situ resulfided with a 4 L/h flux of a 10% mol H_2S/H_2 mixture at 200°C for 4 h. The temperature was then decreased to 30°C under a 4 L/H N_2 flux. The cell temperature was then increased to 200°C (5°C/min) and the system was maintained under high vacuum (P = $1.9.10^{-8}$ bar) for 2 h using a turbomolecular Pfeiffer pump. The temperature was then decreased to 30°C before being isolated from vacuum. Lutidine contained in a capillary tube was then added to the closed cell for 30 min. The pressure was then reduced to 1.10^{-5} bar for 30 min in order to remove the lutidine in excess using an Edwards E2M2 pump. The IR analysis was then performed with 30 µL of lutidine at different temperatures (30, 50, 75 and 100°C). The values of integrated absorbance were obtained using the Perkin Elmer Spectrum software. The Brönsted acidity was measured considering the area of the adsorption band between 1620 and 1660 cm^{-1}. The Lewis acidity was measured using the area of the adsorption band at 1603 cm^{-1} [52]. The integrated absorbance values were reported in function of the temperature of measurement. The methodology used for calculating the concentration of acid sites is similar to the one reported by Emeis [53]. The Lewis and Brönsted acidities were calculated using the following equation:

$$C(x) = IMEC\ (x)^{-1}\ IA(x)\frac{\pi R^2}{m} \qquad (6)$$

where $C(x)$ is the concentration of Brönsted and Lewis acid sites (µmol/g), $IA(x)$ is the value of integrated absorbance, R is the disk radius, m is the catalyst weight and $IMEC\ (x)$ is the integrated molar extinction coefficient for the Brönsted acid sites ($IMEC\ (B)$= 6.8 cm/µmol) and for the Lewis ones ($IMEC\ (L)$ =4.4 cm/µmol) [52].

2.6. Catalytic evaluation

The catalytic activity evaluation of the different samples was performed in a fixed bed continuous flow micro-reactor. A 0.4 ml/min flux of new or waste soybean oil solution (10% v/v in heptane with 0.05 % of dimethyldisulfide, DMDS) as well as a 35 ml/min H_2 flux were fed to the reactor containing 0.01 g of previously sulfided catalyst. The catalysts were indeed first activated by sulfidation with a 4 L/h flux of a 10 mol % H_2S in H_2 mixture at 400°C (5°C/min) for 4 h. The reaction was carried out at temperatures between 380 and 410°C and a 40 Bar H_2 pressure.

The free fatty acid and triglyceride concentrations were measured by infrared spectroscopy. The triglyceride concentration was measured using a linear calibration curve of the area of the C=O stretching vibration band of the ester group at 1750 cm^{-1}. The free fatty acid concentration was determined considering a calibration curve of the area of the C=O stretching band of the carbonyl group at 1714 cm^{-1}.

The products of the deoxygenation reaction were determined by gas chromatography. Based on the reactants, reaction intermediates and products observed in this study, a mechanism was proposed comprising two pseudo-first order consecutive reactions. The kinetic model was developed considering the following assumptions:

1) the hydrogenation reaction occurs at the beginning of the reaction with $k_{HYD}>>>k_1$ and $k_{HYD}>>>k_2$. Therefore, the initial triglyceride concentration (C_{Tgo}) is equal to the concentration of hydrogenated triglycerides (C_{HTgo}) at the beginning of the reaction.

2) the rate constant of the hydrogenolysis reaction (k_1) is higher than the deoxygenation rate constant (k_2) then with $k_1>k_2$,

3) the hydroconversion of hydrogenated triglycerides occurs with two first order consecutive reactions

4) secondary reactions (isomerization, hydrocracking, dehydrogenation and aromatization) do not occur in the kinetic regime but only at high conversions.

The evaluation of the k_1 and k_2 rate constants allows to determine and to compare the activity of the catalysts for the hydroconversion of soybean oil.

The hydrogenolysis reaction was evaluated considering a first order rate (r_1) according to the following equation:

$$-r_1 = k_1\, C_{Tg_0}(1 - x_1) \qquad (7)$$

where k_1 is the hydrogenolysis rate constant ($s^{-1}.g^{-1}$) calculated using equation 8, x_1 is the hydrogenated triglyceride conversion calculated using equation 9, F_{Tg_0} is the molar flux of initial triglycerides ($mol.s^{-1}$), C_{Tg_0} and C_{Tg} are the molar concentrations of triglycerides (mol/L) initially and at equilibrium, m_c is the catalyst weight (g).

$$k_1 = -\frac{F_{Tg_0}}{m_c\, C_{Tg_0}} \ln(1 - x_1) \qquad (8)$$

$$x_1 = \frac{C_{Tg_0} - C_{Tg}}{C_{Tg_0}} \qquad (9)$$

The deoxygenation reaction allows to convert fatty acids in green diesel. The free fatty acid deoxygenation rate (r_2) is of first order and was calculated using equation 10:

$$-r_2 = k_2 C_{FA_0}(1 - x_2) \quad (10)$$

$$x_2 = \frac{C_{FA_0} - C_{FA}}{3C_{Tg_0}} \quad (11)$$

$$k_2 = -\frac{F_{FA_0}}{m_c\, C_{FA_0}} \ln(1 - x_2) \quad (12)$$

where x_2 is the free fatty acid conversion calculated using equation 11, k_2 ($s^{-1}.g^{-1}$) is the rate constant of the free fatty acid deoxygenation reaction calculated using equation 12, F_{FA_0} is the molar flux of free fatty acids initially ($mol.s^{-1}$), C_{FA_0} and C_{FA} are the molar concentrations of free fatty acids (mol/L) initially and at equilibrium, m_c is the catalyst weight (g).

The total yield Y_D (green diesel concentration obtained with respect to the initial triglyceride concentration) was determined as follows:

$$Y_D = \frac{C_{diesel}}{C_{Tg_0}} \quad (13)$$

where C_{diesel} is the alkane concentration obtained indirectly from the concentration of converted free fatty acids (C_{FA_0}-C_{FA}).

The selectivity in hydrocarbons in the green diesel (S_x) was determined as follows:

$$S_x = \frac{A_x}{\sum A_x} \quad (14)$$

where A_x is the area of the peak corresponding to the as-obtained x alkane. The efficiency in hydrodeoxygenation (HDO) with respect to decarboxylation and decarbonylation S_{HDO} was measured as follows:

$$S_{HDO} = \frac{S_{C18}}{S_{C17}} \quad (15)$$

where S_{C18} is the octadecane selectivity and S_{C17} is the heptadecane selectivity.

The % deactivation (%D) due to waste oil is determined as follows:

$$\%D = \frac{Y_{D\,(new\,oil)} - Y_{D\,(waste\,oil)}}{Y_{D\,(new\,oil)}} \quad (16)$$

where Y_D is the total yield with new and waste oil, respectively.

3. Results and discussion

3.1. Characterization of supports

Supports were first characterized by zeta potential in order to determine their net surface pH (Figure 2). The addition of various amounts of manganese can generate different superficial properties. The point of zero charge can be associated with the net surface pH of the support [54]. The sol-gel Al_2O_3 support presents a net surface pH of 8.8 whereas the Al_2O_3-Mn_1 support has a value of 8.7 showing no noticeable differences between these two supports. However, the Al_2O_3-Mn_5 support exhibits a net surface pH of 7.6, then with more acidic properties than the Al_2O_3 and Al_2O_3-MnO_1 supports. The decrease of the net surface pH of the Al_2O_3-Mn_5 support may be associated with a higher amount of Mn^{4+} as in MnO_2 since this latter oxide has an isoelectric point of 4.5 [55].

Figure S1 reports the nitrogen adsorption-desorption isotherms of the three supports. Isotherms are of type IV corresponding to mesoporous solids. Moreover, hysteresis loops are of H1 type. This kind of hysteresis is associated with the presence of uniformly distributed cylindrical pores [56].

Table 1 summarizes the textural properties of the Al_2O_3, Al_2O_3-Mn_1 and Al_2O_3-Mn_5 supports. Specific surface area values do not exhibit a clear trend with the Mn amount while the pore volumes and average pore sizes decrease when increasing the Mn amount. These results may suggest that manganese can block partly the pore apertures of the Al_2O_3 support.

The UV-vis DR spectra of the supports are reported in Figure S2. The Al_2O_3 support does not present bands in the 200-1100 nm interval. The Al_2O_3-Mn_1 support exhibits two bands at 252 nm and 485 nm which are associated respectively to the presence of the $O^{2-} \rightarrow Mn^{2+}$ charge transfer band and to the formation of Mn^{3+} species stabilized on the alumina support (Mn^{3+}-Al_2O_3) [44].

The Al_2O_3-Mn_5 support presents three bands at 265 nm, 380 nm and 471 nm. The 265 nm band is associated with the $O^{2-} \rightarrow Mn^{2+}$ charge transfer band. The 471 nm band corresponds to the presence of Mn^{4+} species stabilized on alumina (Mn^{4+}-Al_2O_3). The 380 nm signal is due to free Mn^{3+} species as in Mn_2O_3.

3.2. Characterization of the impregnation solutions

In order to identify the nature of the different Ni and Mo species that would be able to be deposited onto the surface of the supports, impregnation solutions at pH=5 and pH=9 were

analyzed by UV-vis and Raman spectroscopies. Figure S3 reports the UV-vis spectra of the different impregnation solutions. The UV-vis spectrum of the impregnation solution at pH=5 shows bands at 240 and 300 nm corresponding to a mixture of tetrahedral (T_d) and octahedral (O_h) Mo^{6+} [57]. The octahedral Mo^{6+} (O_h) signal refers to $Mo_7O_{24}^{6-}$ species while the tetrahedral (T_d) one is due to MoO_4^{2-}. Ni species exhibit bands at 370 nm and 400 nm corresponding to $Ni(H_2O)_6]^{2+}$ and at 660 nm and 720 nm bands associated to Ni^{2+} with local octahedral symmetry [$Ni^{2+}6O^{2-}$] [58]. On the other side, the UV-vis spectrum of the impregnation solution at pH=9 shows only few bands. One band in the UV region is found at 250 nm and is associated to the presence of tetrahedral (Td) Mo^{6+} species while octahedral ones only lead to a shoulder around 300 nm. The band observed at 610 nm corresponds to tetrahedral Ni^{2+} (Td) species [58].

Figure 3 reports the Raman spectra of the impregnation solutions. First of all, all the spectra show a contribution at 1048 cm^{-1} due to nitrate ions. The solution at pH=5 presents bands at 944 and 894 cm^{-1} corresponding to Mo=O stretching vibration modes of the $Mo_7O_{24}^{6-}$ ion [57, 58]. On the other side, the spectrum of the solution at pH=9 exhibits two bands at 894 and 830 cm^{-1} due to Mo=O stretching vibrational modes of the MoO_4^{2-} ion with local tetrahedral symmetry. This latter point is corroborated by the presence of a band at 320 nm associated to a Mo=O bending vibrational mode [59].

In conclusion, the solution at pH=5 mainly contains $Mo_7O_{24}^{6-}/Ni^{2+}$(O_h) species while the solution at pH=9 comprises MoO_4^{2-}/Ni^{2+} (T_d) species.

3.3. Characterization of the catalysts at the oxide state

The influence of the pH of the impregnation solution and of the Mn content of the supports on the nature of the Ni and Mo species deposited on dried and calcined catalysts was analyzed by UV-vis diffuse reflectance and Raman spectroscopies. Results were compared to the $NiMo/Al_2O_3$-pH5 and $NiMo/Al_2O_3$-pH9 reference catalysts.

3.3.1. $NiMo/Al_2O_3$ reference catalysts

Figure 4 reports the UV-vis DR spectra of the $NiMo/Al_2O_3$–pH5 and $NiMo/Al_2O_3$–pH9 catalysts at the dried state (D). Both dried catalysts show bands at 280 and 288 nm associated mainly to a mixture of Mo^{6+}(O_h) and Mo^{6+}(T_d) [57]. Moreover, a band at 660 nm is observed in both cases corresponding to octahedral (O_h) Ni^{2+} species [60].

UV-vis DR results of the calcined catalysts are reported in Figure 5. After calcination, two bands are observed at 280 and 310 nm corresponding respectively to tetrahedral and octahedral Mo^{6+} species. Moreover, two signals are found at 710 and 770 nm and are characteristic of octahedrally distorted Ni^{2+} species [44].

The Raman spectra of the NiMo/Al_2O_3–pH5 and NiMo/Al_2O_3–pH9 catalysts at the dried state are shown in Figure S4. The NiMo/Al_2O_3–pH5-D sample exhibits two main bands, one at 1048 cm^{-1} corresponding to the NO_3^- ion and one at 941 cm^{-1} corresponding to the Mo=O stretching vibration of the $Mo_7O_{24}^{6-}$ ion [44, 57]. Moreover, two additional bands of lower intensity at 860 and 840 cm^{-1} are observed and are due to asymmetric Mo-O-Mo stretching vibrations. Identical results are found for NiMo/Al_2O_3–pH9-D.

Figure S5 reports the Raman spectra of the calcined NiMo/Al_2O_3-pH5 and NiMo/Al_2O_3-pH9 catalysts. The Raman spectrum of NiMo/Al_2O_3-pH5-C presents three bands at 944, 860 and 840 cm^{-1} associated with the presence of $Mo_7O_{24}^{6-}$ species. The band at 961 cm^{-1} can be attributed to $Mo_8O_{26}^{4-}$ species [59]. Finally, the signals at 933 cm^{-1} (Mo=O stretching) and 720 cm^{-1} (asymmetric Mo-O-Mo stretching) can be related to MoO_4^- species [59]. Once again, similar conclusions can be reached for NiMo/Al_2O_3-pH9-C.

Based on these UV-vis DR and Raman results, polymerization of Mo species is clearly evidenced after calcination. Predominant species present on NiMo/Al_2O_3-pH5-C and NiMo/Al_2O_3-pH9-C calcined catalysts are octahedral Ni^{2+} species in interaction with $Mo_7O_{24}^{6}$. However, the most important conclusion is also that the pH used for the impregnation solution does not play a significant role since all Ni and Mo species are identical on both dried and calcined catalysts. This suggests that the nature of the Ni and Mo species is here mainly governed by the net surface pH of the Al_2O_3 support.

3.3.2. NiMo catalyst supported on Al_2O_3-Mn_1

Figure 6 reports the UV-vis diffuse reflectance spectra of the dried NiMo/Al_2O_3-Mn_1-pH5-D and NiMo/Al_2O_3-Mn_1-pH9-D catalysts. Both spectra present a main band at 280 nm corresponding to tetrahedral (T_d) Mo^{6+} species [57] with a hardly perceptible shoulder at 252 nm due to Mn^{2+} [61]. Moreover, a band at 478 nm can be observed in both cases resulting from a mixture of Mn^{4+} and Mn^{3+} species stabilized on alumina [44]. Two low intense bands are also found on both catalysts at 660 and 750 nm and correspond respectively to octahedral and distorted octahedral Ni^{2+} species interacting with Mo^{6+} entities. However, a significant difference can be noted when analyzing the NiMo/Al_2O_3-Mn_1-pH9-D sample. Indeed, in this

case, an additional band is observed at 383 nm due to the interaction of free Mn^{3+} species interacting with nickel to form a $NiMn_2O_4$ spinel phase [44].

After calcination, the NiMo/Al_2O_3-Mn_1-pH5-C sample still presents the 280 nm band due to tetrahedral Mo^{6+} species (Figure 7). A new band is also observed at 320 nm due to $O^{2-} \rightarrow Mn^{3+}$ charge transfer band. Additionally, another band which was not observed at the dried state is also found at 420 nm. This band is related to the presence of Mn^{2+} species as in MnO. The appearance of these new manganese bands suggests some migration of manganese species to the surface of the support during calcination [44]. Finally, a weak band at 770 nm is also observed and corresponds to the presence of distorted octahedral Ni^{2+} species.

The NiMo/Al_2O_3-Mn_1-pH9-C sample presents the same contributions at 280 and 320 nm as for NiMo/Al_2O_3-Mn_1-pH5-C. However in the present case, an additional band can be found at 370 nm which is associated to the presence of free Mn^{3+} species as in Mn_2O_3 [44, 58]. Moreover, the NiMo/Al_2O_3-Mn_1-pH9-C UV-vis spectrum presents some unresolved contributions between 380 and 600 nm. In this region, one can expect contributions of Mn^{2+}, Mn^{3+} and Mn^{4+} species in interaction with the support and giving rise to signals respectively at 422, 485 and 470 nm with the Mn^{2+} contribution prevailing. The increasing intensity of these contributions after calcination can be once again due to a migration of manganese to the surface of the support. Finally, the nickel species give rise to two contributions at 680 and 780 nm due respectively to octahedral and distorted octahedral Ni^{2+} species [44, 58].

The Raman spectra of the dried NiMo/Al_2O_3–Mn_1–pH5-D and NiMo/Al_2O_3–Mn_1–pH9–D catalysts are shown in Figure 8. The NiMo/Al_2O_3–Mn_1–pH5-D sample still presents the characteristic signal at 1048 cm^{-1} due to nitrate ions. The broad band with a maximum absorbance at 940 cm^{-1} corresponds to the Mo=O stretching vibration of $Mo_7O_{24}^{6-}$ species. This last assignment can be corroborated by the presence of a band at 340 cm^{-1} associated with the corresponding Mo=O bending vibration. The broad band at 940 cm^{-1} also presents a shoulder centered at 920 cm^{-1} associated with the Mo=O stretching vibration of MoO_4^{2-} species.

The NiMo/Al_2O_3–Mn_1–pH9-D sample exhibits similar bands at 1048, 940 and 920 cm^{-1}. However, one should notice a shift of the Mo=O bending vibration band from 340 to 334 cm^{-1} which is related to a higher proportion of tetrahedral Mo^{6+} like MoO_4^{2-} species in this latter case. Finally, in both catalysts, a band at 229 cm^{-1} can be found corresponding to the deformation vibrational mode of Mo-O-Mo bonds.

Raman spectra of calcined NiMo/Al_2O_3-Mn_1-pH5-C and NiMo/Al_2O_3-Mn_1-pH9-C catalysts are shown in Figure 9. In both cases, calcination leads to the disappearance of the band at 1048 cm^{-1} due to nitrate ions. Moreover, the NiMo/Al_2O_3-Mn_1-pH5-C sample presents two intense bands

associated to Mo=O stretching vibrational modes, one at 947 cm^{-1} due to $Mo_7O_{24}^{6-}$ and one at 933 cm^{-1} due to MoO_4^{2-}. Additional bands at 897 and 850 cm^{-1} related to asymmetric Mo-O-Mo stretching vibrations can also be noted. The presence of $Mo_7O_{24}^{6-}$ species is confirmed by the appearance of a band at 340 cm^{-1}. A shoulder at 320 cm^{-1} can also be corroborated with the presence of MoO_4^{2-} species with tetrahedral coordination. Moreover, a band at 646 cm^{-1} is mainly due to Mn^{3+} species stabilized by alumina [62]. The presence of Mn^{3+} stabilized by alumina can induce important surface structural modifications due to the Jahn-Teller effect like favoring a higher dispersion of nickel species [63, 64].

The Raman spectrum of the NiMo/Al_2O_3–Mn_1-pH9-C sample exhibits similar bands to NiMo/Al_2O_3–Mn_1-pH5-C. However, the Mo=O stretching band slightly shifts from 933 to 925 cm^{-1}.

3.3.3 NiMo catalysts supported on Al_2O_3-Mn_5

UV-vis diffuse reflectance spectra of the dried NiMo/Al_2O_3–Mn_5–pH5-D and NiMo/Al_2O_3–Mn_5–pH9-D catalysts are reported in Figure 10. First of all, as noticed previously in [44], UV-vis diffuse reflectance spectra of Al_2O_3-Mn_5 is dominated by manganese oxide charge transfer bands. The NiMo/Al_2O_3–Mn_5–pH5-D sample shows two bands at 263 and 470 nm corresponding respectively to the $O^{2-} \rightarrow Mn^{2+}$ charge transfer band and to Mn^{4+} species stabilized by the alumina support (Mn^{4+}-Al_2O_3). The 470 nm band also extends to longer wavelengths up to 600 nm suggesting the presence of other Mn species in lower proportions [44]. Moreover, a band at 295 nm can be observed which is associated mainly with octahedral Mo^{6+} species.

The NiMo/Al_2O_3–Mn_5–pH9-D sample shows bands at 272 nm and at 326 nm corresponding to $O^{2-} \rightarrow Mn^{2+}$ and to $O^{2-} \rightarrow Mn^{3+}$ charge transfer bands. The bands at 290 and 308 nm correspond to molybdenum oxide species mainly with local octahedral symmetry. Moreover, the presence of a clear signal at 383 nm is characteristic of the presence of a $NiMn_2O_4$ spinel phase. Finally, clear bands are detected at 420 and 470 nm and are related to the presence of Mn^{2+} and Mn^{4+} species in interaction with alumina (Mn^{2+}-Al_2O_3 and Mn^{4+}-Al_2O_3) [44, 61]. Once again, the 470 nm band tends to extend to higher wavelengths suggesting the presence of other Mn species like Mn^{3+}. This also leads to an overlap with the weak signals expected for nickel making their detection unfeasible in the present case.

Figure 11 reports the UV-vis diffuse reflectance spectra of the calcined NiMo/Al_2O_3–Mn_5-pH5-C and NiMo/Al_2O_3–Mn_5-pH9-C catalysts. After calcination, the NiMo/Al_2O_3–Mn_5-pH5-C sample presents one band at 290 nm due mainly to $O^{2-} \rightarrow Mo^{6+}$ octahedral molybdenum oxide species. A second charge transfer band but due to $O^{2-} \rightarrow Mn^{3+}$ transition can be observed at 320 nm. Two intense bands are also observed at 425 and 470 nm and correspond to Mn^{2+} and Mn^{4+} in interaction with alumina [44, 58]. An important feature on this UV-vis DR spectrum is the presence of a band at 380 nm characteristic of the formation of a $NiMn_2O_4$ spinel phase and resulting from the interaction of free Mn^{3+} species with nickel species. The presence of such a phase is of considerable importance since it leads to a loss of Ni not available as promoter for the MoS_2 phase after sulfidation. Finally, the overlap of Mn signals at high wavelengths with nickel species hampers the detection of these latter compounds.

On the NiMo/Al_2O_3–Mn_5-pH9-C sample, apart from the $O^{2-} \rightarrow Mo^{6+}$ charge transfer band of octahedral molybdenum oxide species at 300 nm, two charge transfer bands due to manganese are observed at 262 nm ($O^{2-} \rightarrow Mn^{2+}$) and at 326 nm ($O^{2-} \rightarrow Mn^{3+}$). Moreover, the bands at 420 and 470 nm due to Mn^{2+} and Mn^{4+} in interaction with alumina are also found. Finally, once again, the signal at 380 nm due to the spinel phase is detected. Weak signals due to nickel cannot be observed.

The Raman spectra of the dried NiMo/Al_2O_3–Mn_5-pH5-D and NiMo/Al_2O_3–Mn_5-pH9-D samples are reported in Figure 12. Both catalysts present similar profiles with a broad band with maximum at 930-933 cm^{-1} characteristic of MoO_4^{2-} species [58]. This last assignment is confirmed by the presence of a band at 328 cm^{-1} due to Mo=O bending vibration of such MoO_4^{2-} species.

Figure 13 reports the Raman results of the calcined NiMo/Al_2O_3–Mn_5-pH5-C and NiMo/Al_2O_3–Mn_5-pH9-C samples. After calcination, the NiMo/Al_2O_3–Mn_5-pH5-C catalyst presents a substantial polymerization of the molybdenum oxide species giving rise to a band at 961 cm^{-1} due to $Mo_8O_{26}^{4-}$ species. The polymerization process resulting from the calcination appears slightly less advanced in the case of the NiMo/Al_2O_3–Mn_5-pH9-C solid with a band centered at 946 cm^{-1} due to $Mo_7O_{24}^{6-}$ species.

Table 2 summarizes the different Mo and Mn species present on the different catalysts. On the reference catalysts without Mn, the main Mo species are $Mo_7O_{24}^{6-}$ whatever the pH of the impregnation solution showing that the net surface pH of the alumina support plays a more definite role in controlling the nature of the main Mo species deposited.

On the catalysts deposited on Al_2O_3-Mn_1, the effect of adding 1% Mn does not really modify the nature of the Mo species present. This result confirms that the net surface pH of the support plays a major role here contrary to the pH of impregnation since here zeta potential measurements shows point-of-zero charge values almost unchanged compared to the Al_2O_3 support without Mn. About manganese species, at the dried state, Mn^{2+} and Mn^{4+} species stabilized by alumina predominate. After calcination, the situation remains relatively similar for NiMo/Al_2O_3-Mn_1-pH5-C while free Mn^{3+} species favoring the formation of the spinel phase are also partly present on NiMo/Al_2O_3-Mn1-pH9-C.

On the catalysts deposited on Al_2O_3-Mn_5, as expected, the change of the net surface pH of the support when adding 5% Mn has effects on the nature of the Mo species at least for NiMo/Al_2O_3-Mn_5-pH5 with the formation of $Mo_8O_{26}^{4-}$ species. About the manganese species, increasing the Mn content to 5 mol % leads to an increased proportion of Mn^{2+} and Mn^{3+} species not stabilized by the alumina support. In this respect, a higher proportion of free Mn^{3+} species is formed on NiMo/Al_2O_3-Mn_5-pH9 than on NiMo/Al_2O_3-Mn_5-pH5. The presence of such free Mn^{3+} species allows the formation of the spinel phase (in higher proportion on NiMo/Al_2O_3-Mn_5-pH9).

3.4. Catalyst characterization at the sulfide state

3.4.1. ICP-OES Analysis and X-ray Photoelectron Spectroscopy

The results obtained by UV-vis diffuse reflectance and Raman spectroscopies for the catalysts at the oxide state suggest that the addition of manganese can influence the distribution of the Ni and Mo species at the surface of the supports after calcination. Moreover, the different Ni and Mo species formed on the calcined catalysts may induce various proportions of promoted NiMoS phase after sulfidation. In order to identify and quantify the different Ni and Mo sulfide species formed after sulfidation, the different sulfided catalysts have been investigated by XPS and ICP-OES.

The results of elemental analysis obtained by ICP-OES are reported in Table 3. The ICP-OES results show a relatively good agreement between the experimental values in Mo, Ni, and Mn and those expected theoretically (Mn= 0.4 wt % and 2.0 wt%, Mo=9.3 wt% and Ni=2.4 wt%). If in the case of nickel, the experimental values are always very close to the theoretical ones, one should note slightly lower experimental values for Mo on the Al_2O_3-Mn_1 support. Similarly, the Mn content is quite close to the theoretical one on the Al_2O_3-Mn_1 support but slightly

deficient on the Al_2O_3-Mn_1 support. Finally, in all cases, the Ni/(Ni+Mo) molar ratio is always equal to the value of 0.30 expected for optimized promotion.

Mo 3d XPS core level spectrum of the NiMo/Al_2O_3-pH5 catalyst is presented in Figure 14 as an example. The NiMo/Al_2O_3-Mn_1-pH5, NiMo/Al_2O_3-Mn_1-pH9, NiMo/Al_2O_3-Mn_5-pH5 and NiMo/Al_2O_3-Mn_5-pH9 catalysts exhibit similar spectra. Mo 3d core level spectra present for each species two Mo $3d_{5/2}$ and Mo $3d_{3/2}$ doublets. Spectra decomposition allows to distinguish three different species: Mo^{4+} as in MoS_2 with the two doublets at binding energies of 229.0 and 232.0 eV, Mo^{5+} as in MoO_xS_y oxysulfides with binding energies at 230.0 and 233.4 eV, and finally Mo^{6+} as in MoO_x with binding energies at 232.1 and 235.3 eV. One should note also the presence of a signal at 226.6 eV due to the S 2s contribution.

Figure 15 reports an example of decomposition of the Ni $2p_{3/2}$ core level spectrum for the NiMo/Al_2O_3-pH5 catalyst. The NiMo/Al_2O_3-Mn_1-pH5, NiMo/Al_2O_3-Mn_1-pH9, NiMo/Al_2O_3-Mn_5-pH5 and NiMo/Al_2O_3-Mn_5-pH9 show similar spectra. The Ni $2p_{3/2}$ core level region comprises three main contributions: 1) the non-promoted NiS_x phase with a binding energy at 852.7 eV, 2) the promoted NiMoS phase with a binding energy at 853.8 eV, and finally 3) the NiO_x phase with a binding energy at 855.4 eV. Contributions at 856.5, 859.4 and 861.9 eV are due to shake-up satellites.

The results of the Mo 3d and Ni 2p core level spectra decomposition are shown in Table 4. The Mo 3d decomposition results do not show any significant variations among all the different catalysts investigated with for instance the MoS_2 proportion remaining similar in all cases (71-78%). About Ni 2p core level decomposition results, adding 1% Mn does not modify the proportion of the promoted phase (around 70%) compared to the NiMo/Al_2O_3-pH5 reference. One should only note a lower proportion of non-sulfided NiO_x phase for the NiMo catalysts supported on Al_2O_3-Mn_1 but without consequences on the proportion of promoted phase. On the contrary, the addition of 5% Mn leads to a decrease of the proportion of the promoted phase to 62% for NiMo/Al_2O_3-Mn_5-pH5 and to 54% for NiMo/Al_2O_3-Mn_5-pH9. This last result can be related to the formation of the $NiMn_2O_4$ spinel phase observed at the oxide state and limiting the availability of nickel to promote MoS_2 slabs [44].

3.4.2. High resolution transmission electron microscopy (HRTEM) results

HRTEM analysis allows to evaluate the influence of the addition of manganese to the Al_2O_3 support on the dispersion and morphology of the MoS_2 particles. Statistical results of the HRTEM analysis are reported in Table 5. Note that the HRTEM analysis was not performed on

the NiMo/Al_2O_3-Mn_5-pH9 solid due to its poor catalytic performances (vide infra). The statistical analysis was performed for each catalyst on 600-800 particles counted on 10 different micrographs (area of 5170 nm^2).

The addition of 1% Mn does not modify significantly the average stacking degree of the MoS_2 slabs by comparison to the NiMo/Al_2O_3-pH5 reference. However, a significant influence on the average slab length can be noticed with values around 2.3 nm versus 2.9 nm for the reference. This higher degree of dispersion can be related to the more important stabilization of manganese species on the alumina support (Table 2) at least at the dried state for both NiMo/Al_2O_3-Mn_1-pH5 and NiMo/Al_2O_3-Mn_1-pH9 catalysts and for NiMo/Al_2O_3-Mn_1-pH5 at the calcined state. This also results in a higher density of stacks per 1000 nm^2 for NiMo/Al_2O_3-Mn_1-pH5 (14.2) while a lower value of 11.4 was found for NiMo/Al_2O_3-Mn_1-pH9 probably due to a higher destabilization of Mn species as reflected by the appearance of a signal due to free Mn^{3+} species (Table 2).

On the opposite, adding 5% Mn leads to average stacking degree and slab length similar to the NiMo/Al_2O_3-pH5 reference showing that an excess of Mn by increasing the proportion of manganese species which are not stabilized by alumina contributes to the loss of any beneficial effect on the dispersion of the active phase.

3.4.3. Analysis of the acid properties by lutidine adsorption followed by infrared spectroscopy.

The acidity of the different catalysts at the sufide state was studied using Fourier transform infrared spectroscopy with lutidine as probe molecule. The *ν*(8b) and *ν*(8a) vibrational modes of lutidine and of the lutidinium ion (in-plane vibrations of the C6 aromatic ring) are generally used for the analysis of the Brönsted and Lewis sites by infrared spectroscopy. The 1603 cm^{-1} band is associated with the Lewis acid sites while the bands at 1620 and 1640 cm^{-1} are related to Brönsted acid sites [50-52]. As an example, the FTIR spectra of adsorbed lutidine on the NiMo/Al_2O_3-pH5 catalysts are reported Figure 16 in function of the temperature of desorption. Both bands due to Brönsted acidity (between 1620 and 1660 cm^{-1}) and to Lewis acidity (1603 cm^{-1}) can be detected for NiMo/Al_2O_3-pH5. The band at 1585 cm^{-1} is associated to lutidine adsorption through H-bonding.

Based on the different recorded FTIR spectra and using the methodology of Emeis [53], the concentrations of Brönsted and Lewis acid sites were calculated for each catalyst at the different temperatures of desorption of lutidine. One should note that the concentration in Brönsted acid

sites does not change with the increasing desorption temperature contrary to what is observed for the Lewis acid sites. Therefore, Figure 17 reports the evolution of the concentration of Lewis acid sites in function of the lutidine desorption temperature for each catalyst.

At a temperature of desorption of 30°C, the NiMo/Al_2O_3-pH5 and NiMo/Al_2O_3-Mn_1-pH5 catalysts exhibit similar concentration of Lewis acid sites (29 and 26 µmol/g respectively). On the opposite, the NiMo/Al_2O_3-Mn_5-pH5 catalyst presents a lower amount of Lewis acid sites (15 µmol/g). A similar effect can be noticed Figure S6 for the same series of catalysts but following an impregnation at pH=9. Moreover, with the increasing temperature of desorption, the amount of Lewis acid sites on the NiMo/Al_2O_3-Mn_5-pH5 and NiMo/Al_2O_3-Mn_5-pH9 catalysts decreases less rapidly than for the other two series of catalysts (reference without Mn and supported on Al_2O_3-Mn_1) suggesting a higher Lewis acid strength of the sites located on Al_2O_3-Mn_5. This effect can be related to the significant migration at the surface of the support of manganese oxide species in the case of the addition of 5 mol% as observed by UV-vis DR results. This would suggest the replacement on the surface of the catalysts of Lewis acid sites due to alumina by those coming from manganese oxide species in lower amount but with a higher strength. On the contrary, for NiMo catalysts supported on Al_2O_3-Mn_1, the migration of manganese species remains much more limited as shown by UV-vis DR results leading to acid properties closer to those observed for the NiMo/Al_2O_3 reference catalysts.

The concentrations of Lewis and Brönsted acid sites after desorption at 30°C are summarized in Table 6. The addition of 1% Mn to the Al_2O_3 support does not lead to any significant variation in Lewis acid site concentration. On the opposite, the amount of Brönsted acid sites decreases by 40% for NiMo/Al_2O_3-Mn_1-pH5 and NiMo/Al_2O_3-Mn_1-pH9 compared to the reference catalysts without Mn. Moreover, the addition of 5% Mn leads to a significant decrease of both Lewis and Brönsted acid concentrations. While the NiMo/Al_2O_3-Mn_5-pH5 catalyst shows a 50% decrease of the Lewis acidity concentration, the amount of Lewis acid sites on NiMo/Al_2O_3-Mn_5-pH9 diminishes in a lower extent by 20%. The decrease in Brônsted acidity concentration appears here more drastic with losses respectively of 67% and 50% for NiMo/Al_2O_3-Mn_5-pH5 and NiMo/Al_2O_3-Mn_5-pH9.

3.5. Catalytic hydroconversion of soybean oil

In order to evaluate the effect of the addition of manganese to the alumina support as well as the influence of the pH of the impregnation solutions, the different NiMo catalysts supported on Al_2O_3-Mn_1 and on Al_2O_3-Mn_5 were tested by comparison to the NiMo/Al_2O_3 reference

catalysts for the catalytic hydroconversion of new and waste soybean oil. Table 7 reports for each catalyst the results for the conversion of triglycerides (x_1) and of free fatty acids (x_2), the green diesel Y_D yield, as well as the deactivation parameter (D). Results show undoubtedly the superiority of the NiMo catalysts supported on Al_2O_3-Mn_1 whatever the pH of impregnation solution. The triglyceride conversion (x_1) of new soybean oil decreases in the following order: NiMo/Al_2O_3-Mn_1-pH5 > NiMo/Al_2O_3-Mn_1-pH9 > NiMo/Al_2O_3-Mn_5-pH5 > NiMo/Al_2O_3-pH5 ≈ NiMo/Al_2O_3-pH9 > NiMo/Al_2O_3-Mn_5-pH9. Using the waste soybean oil, the triglyceride conversion follows: NiMo/Al_2O_3-Mn_1-pH5 > NiMo/Al_2O_3-Mn_1-pH9 > NiMo/Al_2O_3-pH5 > NiMo/Al_2O_3-pH9 > NiMo/Al_2O_3-Mn_5-pH5 > NiMo/Al_2O_3-Mn_5-pH9.

The situation differs when using 5% Mn. The NiMo/Al_2O_3-Mn_5-pH5 catalysts still presents a higher triglyceride conversion than the reference catalysts for new soybean oil even if lower than for the NiMo catalysts supported on Al_2O_3-Mn_1. However, with waste soybean oil, the conversion of NiMo/Al_2O_3-Mn_5-pH5 severely drops. Moreover, in any case (new or waste soybean oil), the NiMo/Al_2O_3-Mn_5-pH9 catalyst presents a poor triglyceride conversion. This last result can be correlated to the formation of the $NiMn_2O_4$ spinel phase resulting in a lower proportion of the NiMoS promoted phase, formation being even higher on NiMo/Al_2O_3-Mn_5-pH9 than on NiMo/Al_2O_3-Mn_5-pH5. Concerning the severe loss of conversion of NiMo/Al_2O_3-Mn_5-pH5 when passing from new to waste soybean oil, this can result from the higher Lewis acid strength of the Al_2O_3-Mn5 support as shown by lutidine adsorption which would favor coke formation when using waste soybean oil.

In terms of free fatty acids conversion (x_2), the same tendency was observed with both new and waste soybean oils with NiMo catalysts supported on Al_2O_3-Mn_1 showing a higher conversion whatever the pH of impregnation used. The NiMo/Al_2O_3-Mn_5-pH5 still presents a severe loss in conversion when passing from new to waste soybean oil even if its conversion remains higher than for the reference catalysts with waste soybean oil. Finally, the NiMo/Al_2O_3-Mn_5-pH9 catalysts exhibits very poor performance particularly with the waste soybean oil.

These last results are also confirmed when considering the green diesel yield (Y_D) with values much higher with the NiMo catalysts supported on Al_2O_3-Mn_1 (0.80-0.82) than on NiMo/Al_2O_3-pH5 (0.51) using new soybean oil. Similar observations can be made with the waste soybean oil (0.60-0.65 vs 0.24). The NiMo/Al_2O_3-Mn_5-pH5 also presents a higher Y_D value with new soybean oil (0.72) but loses any advantage on the reference catalysts with waste soybean oil. Finally, the NiMo/Al_2O_3-Mn_5-pH9 performs particularly poorly with waste soybean oil (0.09).

The deactivation (D) values also show a lower tendency to deactivate for the NiMo catalysts supported on Al_2O_3-Mn_1 than for the reference catalysts while the NiMo catalysts supported on Al_2O_3-Mn_5 strongly deactivate confirming the harmful effect related to the increased Lewis acid strength of these latter catalysts.

The rate constants, k_1 for the hydrogenolysis of triglycerides into free fatty acids and k_2 for the deoxygenation of free fatty acids into hydrocarbons were also determined for each catalyst was well as the corresponding activation energies Ea_1 and Ea_2. Results are reported in Table 8. The evolution of the rate constant values confirm the previous observations with a clear superiority of NiMo catalysts supported on Al_2O_3-Mn_1 using both new and waste soybean oil. The analysis of Table 8 however shows a better activity of NiMo/Al_2O_3-Mn_1-pH5 than NiMo/Al_2O_3-Mn_1-pH9 for the first step, the hydrogenolysis of triglycerides into free fatty acids while activities are similar for the deoxygenation of free fatty acids into hydrocarbons. The NiMo/Al_2O_3-Mn_5-pH5 catalyst loses any beneficial effect when using waste soybean oil with rate constants even lower than for the reference catalysts. Finally, the NiMo/Al_2O_3-Mn_5-pH9 catalyst almost loses any activity for the deoxygenation of free fatty acid into hydrocarbons using waste soybean oil. Finally, the analysis of activation energy values does not show any striking variation when passing from new to waste soybean oil suggesting an absence of modification of the nature of the active sites when changing the nature of the oil.

The nature of the different hydrocarbons formed during the deoxygenation of free fatty acids was analyzed by gas chromatography and results are reported in Table S1. Only linear hydrocarbons from C18 to C15 were obtained. The main effect observed is related to the pH of impregnation used for preparing the NiMo catalysts supports on Mn-containing Al_2O_3. Indeed, whatever the Mn amount, NiMo catalysts prepared at a pH of impregnation of 9 show a better HDO selectivity in C18 hydrocarbons using new soybean oil. However, this effect is lost when using waste soybean oil. One should also note a higher selectivity in pentadecane with NiMo/Al_2O_3-Mn_5-pH9 probably related to the higher acid strength of this latter catalyst.

5. Conclusion

In the present study, the interest of adding manganese to an Al_2O_3 support was evaluated in order to obtain new supported NiMo catalysts for the hydroconversion of new and waste soybean oils. Two different Mn contents were used (1 or 5 mol % Mn as MnO) while two different pHs of impregnation (5 and 9) were employed for preparing the supported NiMo catalysts. The catalytic systems were then investigated at both the oxide and sulfide states. The

pH of impregnation plays a minor role on the nature of the Mo and Ni species deposited on the different supports since the net surface pH of the support mainly governs the distribution of Mo and Ni species to be obtained. While adding 1% Mn to Al_2O_3 results in the stabilization of various Mn oxide species on the alumina support, adding 5% Mn results in the formation of free Mn^{2+} and Mn^{3+} species, not stabilized by the support. Mn^{3+} species are then available to react with nickel to form a $NiMn_2O_4$ spinel which limits the possibility for nickel to form a promoted NiMoS phase as revealed by XPS. Adding 1% Mn also helps to better disperse the Ni-promoted MoS_2 active phase.

The analysis of new and waste soybean oil hydroconversion results shows clearly the superiority of NiMo catalysts if supported on Al_2O_3 with 1% Mn added for both new and waste soybean oils, for both triglyceride hydrogenolysis and fatty acid deoxygenation. On the contrary, NiMo catalysts supported on Al_2O_3 with 5% Mn suffer from lower activities due to the formation of the $NiMn_2O_4$ spinel phase limiting the formation of the NiMoS active phase and from severe deactivation when using waste soybean oil.

Acknowledgements

The authors gratefully acknowledge for their financial support ECOS Nord through programs referenced M16P01 (France) and referenced No. 275186 (ANUIES-CONACYT, Mexico) and No. 256345/CB-2015-01.

References

[1] G.W. Huber, P. O'Connor, A. Corma, Appl. Catal. A 329 (2007) 120-129.

[2] G. Knothe, Prog. Energ. Combust. 36 (2010) 364-373.

[3] S. Bezergianni, A. Dimitriadis, Renew. Sust. Energ. Rev. 21 (2013) 110-116.

[4] B.E.H.P. Freedman, E.H. Pryde, T.L. Mounts, J. Am. Oil Chem. Soc. 61 (1984) 1638-1643.

[5] M. Ameen, M.T. Azizan, S. Yusup, A. Ramli, M. Yasir, Renew. Sust. Energ. Rev. 80 (2017) 1072-1088.

[6] A. Ishihara, N. Fukui, H. Nasu, T. Hashimoto, Fuel 134 (2014) 611-617.

[7] M.F. Wagenhofer, E. Baráth, O.Y. Gutiérrez, J.A. Lercher, ACS Catal. 7 (2017) 1068-1076.

[8] S.K. Kim, J.Y. Han, H.S. Lee, T. Yum, Y. Kim, J. Kim, Appl. Energ. 116 (2014) 199-205.

[9] H. Zhang, H. Lin, Y. Zheng, Appl. Catal. B 160 (2014) 415-422.

[10] R. Sotelo-Boyas, Y. Liu, T. Minowa, Ind. Eng. Chem. Res. 50 (2010) 2791-2799.
[11] M. Anand, A.K. Sinha, Bioresource Technol. 126 (2012) 148-155.
[12] J. Mikulec, J. Cvengroš, L. Joríková, M. Banič, A. Kleinová, J. Clean. Prod. 18 (2010) 917-926.
[13] E. Kordouli, L. Sygellou, C. Kordulis, K. Bourikas, A. Lycourghiotis, Appl. Catal. B 209 (2017) 12-22.
[14] V. Itthibenchapong, A. Srifa, R. Kaewmeesri, P. Kidkhunthod, K. Faungnawakij, Energ. Convers. Manage. 134 (2017) 188-196.
[15] J. Hancsók, T. Kasza, S. Kovács, P. Solymosi, A. Holló, J. Clean. Prod. 34 (2012) 76-81.
[16] R. Kumar, S.A. Farooqui, M. Anand, R. Kumar, R. Joshi, A. Khan, A.K. Sinha, Catal. Comm. 98 (2017) 102-106.
[17] B. Rozmysłowicz, P. Mäki-Arvela, S. Lestari, O.A. Simakova, K. Eränen, I.L. Simakova, T.O. Salmi, Top. Catal. 53 (2010) 1274-1277.
[18] T. Morgan, D. Grubb, E. Santillan-Jimenez, M. Crocker, Top. Catal. 53 (2010) 820-829.
[19] L. Zhou, A. Lawal, Appl. Catal. A 532 (2017) 40-49.
[20] R. Sotelo-Boyas, Y. Liu, T. Minowa, Ind. Eng. Chem. Res. 50 (2010) 2791-2799.
[21] N.A. Grosso-Giordano, T.R. Eaton, Z. Bo, S. Yacob, C.C. Yang, J.M. Notestein, Appl. Catal. B 192 (2016) 93-100.
[22] S. Liu, Q. Zhu, Q. Guan, L. He, W. Li, Bioresour. Technol. 183 (2015) 93-100
[23] T. Morgan, D. Grubb, E. Santillan-Jimenez, M. Crocker, Top. Catal. 53 (2010) 820-829
[24] Y. Duan, R. Ding, Y. Shi, X. Fang, H. Hu, M. Yang, Y. Wu, Catalysts 7 (2017) 81.
[25] I. Hachemi, N. Kumar, P. Mäki-Arvela, J. Roine, M. Peurla, J. Hemming, J. Salonen, D. Y. Murzin,. J. Catal. 347 (2017) 205-221.
[26] Y. Yang, J. Chen, H. Shi, Energy Fuels 27 (2013) 3400-3409.
[27] H. Ren, W. Yu, M. Salciccioli, Y. Chen, Y. Huang, K. Xiong, D. G. Vlachos, J. G. Chen, ChemSusChem, 6 (2013) 798-801. [28] N.Y. Topsøe, A. Tuxen, B. Hinnemann, J.V. Lauritsen, K.G. Knudsen, F. Besenbacher, H. Topsøe, J. Catal. 279 (2011) 337-351.
[29] B. Hinnemann, J.K. Nørskov, H. Topsøe J. Phys. Chem. B 109 (2005) 2245–2253.
[30] J.V. Lauritsen, M. Nyberg, J.K. Nørskov, B.S. Clausen, H. Topsøe, E. Laegsgaard, F. Besenbacher, J. Catal. 224 (2004) 94–106.
[31] N.Y. Topsøe, A. Tuxen, B. Hinnemann, J.V. Lauritsen, K.G. Knudsen, F. Besenbacher, H. Topsøe, J. Catal. 279 (2011) 337–351.
[32] P.G. Moses, B. Hinnemann, H. Topsøe, J.K. Nørskov, J. Catal. 248 (2007) 188–203.
[33] P.G. Moses, B. Hinnemann, H. Topsøe, J.K. Nørskov, J. Catal. 268 (2009) 201–208.

[34] A. Tuxen, H.G. Föchtbauer, B. Temel, B. Hinnemann, H. Topsøe, K.G. Knudsen, F. Besenbacher, J.V. Lauritsen, J. Catal. 295 (2012) 146–154.
[35] L.S. Byskov, J.K. Nørskov, B.S. Clausen, H. Topsøe, Catal. Lett. 64 (2000) 95–99.
[36] J.V. Lauritsen, S. Helveg, E. Laegsgaard, I. Stensgaard, B.S. Clausen, H. Topsøe, F. Besenbacher, J. Catal. 197 (2001) 1–5.
[37] S. Rangarajan, M. Mavrikakis, ACS Catal. 7 (2016) 501-509.
[38] I. Vázquez-Garrido, A. López-Benítez, G. Berhault, A. Guevara-Lara, Fuel 236 (2019) 55-64.
[39] B. Veriansyah, J.Y. Han, S.K. Kim, S.A. Hong, Y.J. Kim, J.S. Lim, Y.W. Shu, S.G. Oh, J. Kim, Fuel 94 (2012) 578-585.
[40] M. Toba, Y. Abe, H. Kuramochi, M. Osako, T. Mochizuki, Y. Yoshimura, Catal. Today 164 (2011) 533-537.
[41] O. Senol, T.R. Viljava, A.O.I. Krause, Catal. Today 106 (2005) 186-189.
[42] E.W. Qian, N. Chen, S. Gong, J. Mol. Catal. A 387 (2014) 76-85.
[43] A.E. Coumans, E.J.M. Hensen, Catal. Today 298 (2017) 181-189.
[44] A. López-Benítez, G. Berhault, A. Guevara-Lara, Appl. Catal. B 213 (2017) 28-41.
[45] A.D. Gandubert, C. Legens, D. Guillaume, E. Payen, Surf. Interf. Analysis 38 (2006) 206-209.
[46] P.C. Yen, Y.S. Huang, K.K. Tiong, J. Phys.: Cond. Matter 16 (2004) 2171-2180.
[47] Y. Okamoto, T. Imanaka, S. Teranishi, J. Catal. 65 (1980) 448-460.
[48] T. Weber, J.C. Muijsers, J.H.M.C. Van Wolput, C.P.J. Verhagen, J.W. Niemantsverdriet, J. Phys. Chem. 100 (1996) 14144-14150.
[49] E. Payen, R. Hubaut, S. Kasztelan, O. Poulet, J. Grimblot, J. Catal. 147 (1994) 123-132.
[50] G. Berhault, M. Lacroix, M. Breysse, F. Maugé, J.C. Lavalley, H. Nie, L. Qu, J. Catal. 178 (1998) 555-565.
[51] M. Breysse, G. Berhault, S..Kasztelan, M. Lacroix, F. Maugé, G. Perot, Catal. Today 66 (2001) 15-22.
[52] T. Onfroy, G. Clet, M. Houalla, Microp. Mesop. Mater. 82 (2005) 99-104.
[53] C.A. Emeis, J. Catal. 141 (1993) 347-354.
[54] R.J. Hunter, in: Zeta potential in colloid science: principles and applications (Vol. 2). Academic press, 2013.
[55] T. Morimoto, S. Kittaka, Bull. Chem. Soc. Japan 47 (1974) 1586-1588.
[56] G. Leofanti, M. Padovan, G. Tozzola, B. Venturelli, Catal. Today 41 (1998) 207-219.
[57] H. Jeziorowski, H. Knözinger, J. Phys. Chem. 83 (1979) 1166-1173.

[58] A. Guevara-Lara, R. Bacaud, M. Vrinat, Appl. Catal. A 328 (2007) 99-108.
[59] G. Mestl, T.K.K. Srinivasan, Catal. Rev. 40 (1998) 451-570.
[60] F. Iova, A. Trutia, Optical Mater. 13 (2000) 455-458.
[61] S. Velu, N. Shah, T.M. Jyothi, S. Sivasanker, Microp. Mesop. Mater. 33 (1999) 61-75.
[62] D.T. Zahn, Phys. Chem. Chem. Phys. 1 (1999) 185-190.
[63] D.M. Robinson, Y.B. Go, M. Mui, G. Gardner, Z. Zhang, D. Mastrogiovanni, E. Garfunkel, J. Li, M. Greenblatt, G.C. Dismukes, J. Am. Chem. Soc. 135 (2013) 3494-3501.
[64] W. Han, F. Dong, W. Han, Z. Tang, New J. Chem. 43 (2019) 12846-12857.

Table 1. Textural properties of the different supports.

% mol Mn	BET surface area (m^2/g)	Pore volume (cm^3/g)	Average Pore Size (nm)
0	385	1.9	8
1	317	1.6	8
5	358	1.4	6

Table 2. Summary of the Mn and Mo species present on the different catalysts.

Catalyst	Dried	Calcined
NiMo/Al_2O_3-pH9	$Mo_7O_{24}^{6-}$	Mainly $Mo_7O_{24}^{6-}$
NiMo/Al_2O_3-pH5	$Mo_7O_{24}^{6-}$	$Mo_7O_{24}^{6-}$
NiMo/Al_2O_3-Mn_1-pH9	$Mo_7O_{24}^{6-}$	MoO_4^{2-} + $Mo_7O_{24}^{6-}$
	Mn^{2+}- Al_2O_3	Mn^{3+}
	Mn^{4+}-Al_2O_3	Mn^{2+}- Al_2O_3
	Spinel	
NiMo/Al_2O_3-Mn_1-pH5	$Mo_7O_{24}^{6-}$	MoO_4^{2-}+ $Mo_7O_{24}^{6-}$
	Mn^{2+}-Al_2O_3	Mn^{3+}
	Mn^{4+}-Al_2O_3	Mn^{2+}-Al_2O_3
NiMo/Al_2O_3-Mn_5-pH9	MoO_4^{2-}	$Mo_7O_{24}^{6--}$
	Mn^{2+}, Mn^{3+}	Mn^{2+}, Mn^{3+}
	Mn^{2+}-Al_2O_3	Mn^{2+}-Al_2O_3
	Mn^{4+}-Al_2O_3	Mn^{4+}-Al_2O_3
	Spinel	Spinel (higher than at pH 5)
NiMo/Al_2O_3-Mn_5-pH5	MoO_4^{2-}	$Mo_8O_{26}^{4-}$
	Mn^{2+}	Mn^{3+}
	Mn^{2+}-Al_2O_3	Mn^{2+}-Al_2O_3
	Mn^{4+}-Al_2O_3	Mn^{4+}-Al_2O_3
		Spinel

Table 3. Ni, Mo and Mn amounts as well as the Ni/(Ni+Mo) atomic ratio determined by ICP-OES for the different NiMo catalysts supported on Al_2O_3-Mn_1 and Al_2O_3-Mn_5 supports. Results for NiMo/Al_2O_3-pH5 are given for comparison purposes.

Catalyst	ICP-OES			
	Mo (wt%)	Ni (wt%)	Mn (wt%)	Ni/(Ni+Mo)
NiMo/Al_2O_3-pH5	8.2	2.1	0.0	0.30
NiMo/Al_2O_3-Mn_1-pH5	7.7	2.1	0.3	0.31
NiMo/Al_2O_3-Mn_1-pH9	7.5	2.1	0.3	0.31
NiMo/Al_2O_3-Mn_5-pH5	9.1	2.5	1.5	0.31
NiMo/Al_2O_3-Mn_5-pH9	9.1	2.4	1.5	0.30

Table 4. Results of the decomposition of the Mo 3d and Ni 2p core level spectra.

Catalyst	$Mo3d_{5/2}$ (%)			$Ni2p_{3/2}$ (%)		
	MoS_2	MoO_xS_y	MoO_x	NiS_x	NiMoS	NiO_x
$NiMo/Al_2O_3$-pH5	76	14	10	7	70	23
$NiMo/Al_2O_3$-Mn_1-pH5	71	16	13	19	68	13
$NiMo/Al_2O_3$-Mn_1-pH9	73	18	9	10	69	21
$NiMo/Al_2O_3$-Mn_5-pH5	78	16	6	21	62	17
$NiMo/Al_2O_3$-Mn_5-pH9	76	14	10	26	54	20

Table 5. Density of stacks per 1000 nm^2, average number of layers per stack $\bar{N}$ and slab length L of different NiMo catalysts supported on Mn-containing alumina. Comparison to the NiMo/Al_2O_3-pH5 reference.

Catalyst	**Stacks per 1000 nm^2**	$\bar{N}$	$\bar{L}(nm)$
NiMo/Al_2O_3-pH5	10.9	1.56	2.91
NiMo/Al_2O_3-Mn_1-pH5	14.2	1.53	2.36
NiMo/Al_2O_3-Mn_1-pH9	11.4	1.47	2.28
NiMo/Al_2O_3-Mn_5-pH5	12.4	1.68	2.79

Table 6. Concentration of Lewis (C_{LA}) and Brönsted (C_{BA}) acid sites, total acid concentrations, and C_{BA}/C_{LA} ratios for the NiMo catalysts supported on Al_2O_3, Al_2O_3-Mn_1, Al_2O_3-Mn_5 following impregnations at pH=5 and pH=9. Values are determined at a temperature of desorption at 30°C with 30 µL of lutidine.

Catalyst	C_{LA} (µmol/g) 1603 cm^{-1}	C_{BA} (µmol/g) 1620-1660 cm^{-1}	Total Acidity (µmol/g)	C_{BA}/C_{LA}
NiMo/Al_2O_3-pH5	29	18	48	0.60
NiMo/Al_2O_3-pH9	26	14	40	0.53
NiMo/Al_2O_3-Mn_1-pH5	26	11	37	0.42
NiMo/Al_2O_3-Mn_1-pH9	27	9	36	0.30
NiMo/Al_2O_3-Mn_5-pH5	15	6	21	0.40
NiMo/Al_2O_3-Mn_5-pH9	22	7	29	0.32

Table 7. Conversions of triglycerides (x_1) and of free fatty acids (x_2), green diesel yield (Y_D), and deactivation (D) values for the NiMo catalysts supported on Al_2O_3-Mn_1 and on Al_2O_3-Mn_5. Comparison to the NiMo/Al_2O_3 reference catalysts (T = 380° C, P = 40 bars).

Catalyst	x_1		x_2		Y_D		%D
	New	Waste	New	Waste	New	Waste	
NiMo/Al_2O_3-pH5	34.7	38.0	17.3	8.0	0.51	0.24	52
NiMo/Al_2O_3-pH9	33.6	26.5	12.9	7.2	0.39	0.26	36
NiMo/Al_2O_3-Mn_1-pH5	48.8	43.8	27.3	20.1	0.82	0.60	27
NiMo/Al_2O_3-Mn_1-pH9	42.1	41.3	26.8	21.5	0.80	0.65	19
NiMo/Al_2O_3-Mn_5-pH5	38.7	25.2	24.1	10.8	0.72	0.32	56
NiMo/Al_2O_3-Mn_5-pH9	29.6	20.2	18.4	2.9	0.55	0.09	83

Table 8. Rate constants k_1 (hydrogenolysis of triglycerides into free fatty acids) and k_2 (deoxygenation of free fatty acids into hydrocarbons) and the respective activation energies (Ea_1 and Ea_2) for the hydroconversion of new and waste soybean oils.

Catalyst	k_1 (10^{-4} $g^{-1}.s^{-1}$)		Ea_1 ($kJ.mol^{-1}$)		k_2 (10^{-4} $g^{-1}.s^{-1}$)		Ea_2 ($kJ.mol^{-1}$)	
	New	Waste	New	Waste	New	Waste	New	Waste
$NiMo/Al_2O_3$-pH5	2.8	2.6	30	38	1.3	1.1	7	24
$NiMo/Al_2O_3$-pH9	2.7	2.1	40	42	0.9	0.5	31	30
$NiMo/Al_2O_3$-Mn_1-pH5	4.5	3.8	50	54	2.1	1.5	13	17
$NiMo/Al_2O_3$-Mn_1-pH9	3.6	3.5	50	51	2.1	1.6	19	26
$NiMo/Al_2O_3$-Mn_5-pH5	3.3	1.9	39	42	1.8	0.8	12	21
$NiMo/Al_2O_3$-Mn_5-pH9	2.3	1.5	34	38	1.3	0.2	D*	D*

*D: this catalysts deactivates in two hours of reaction.

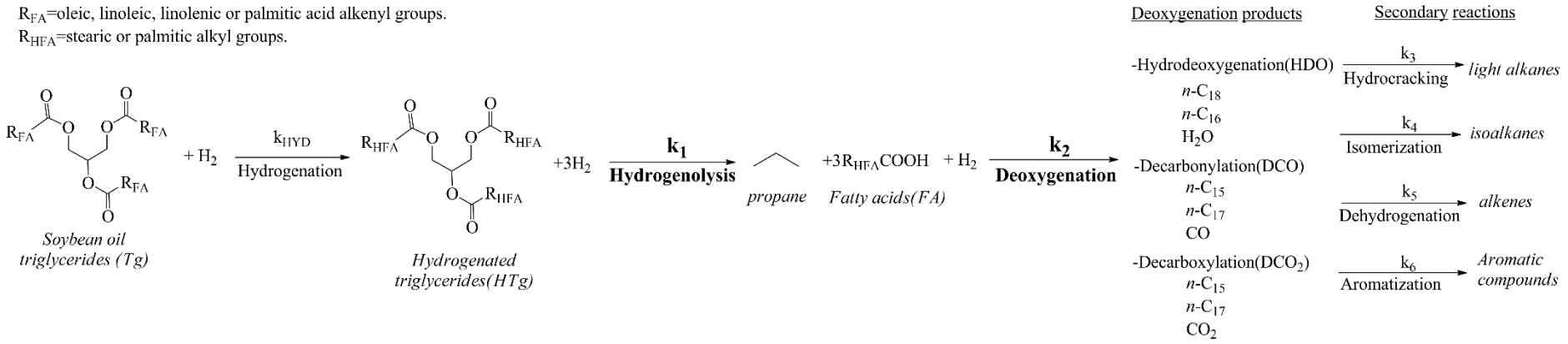

Figure 1. Reaction scheme for the formation of green diesel from soybean oil triglycerides.

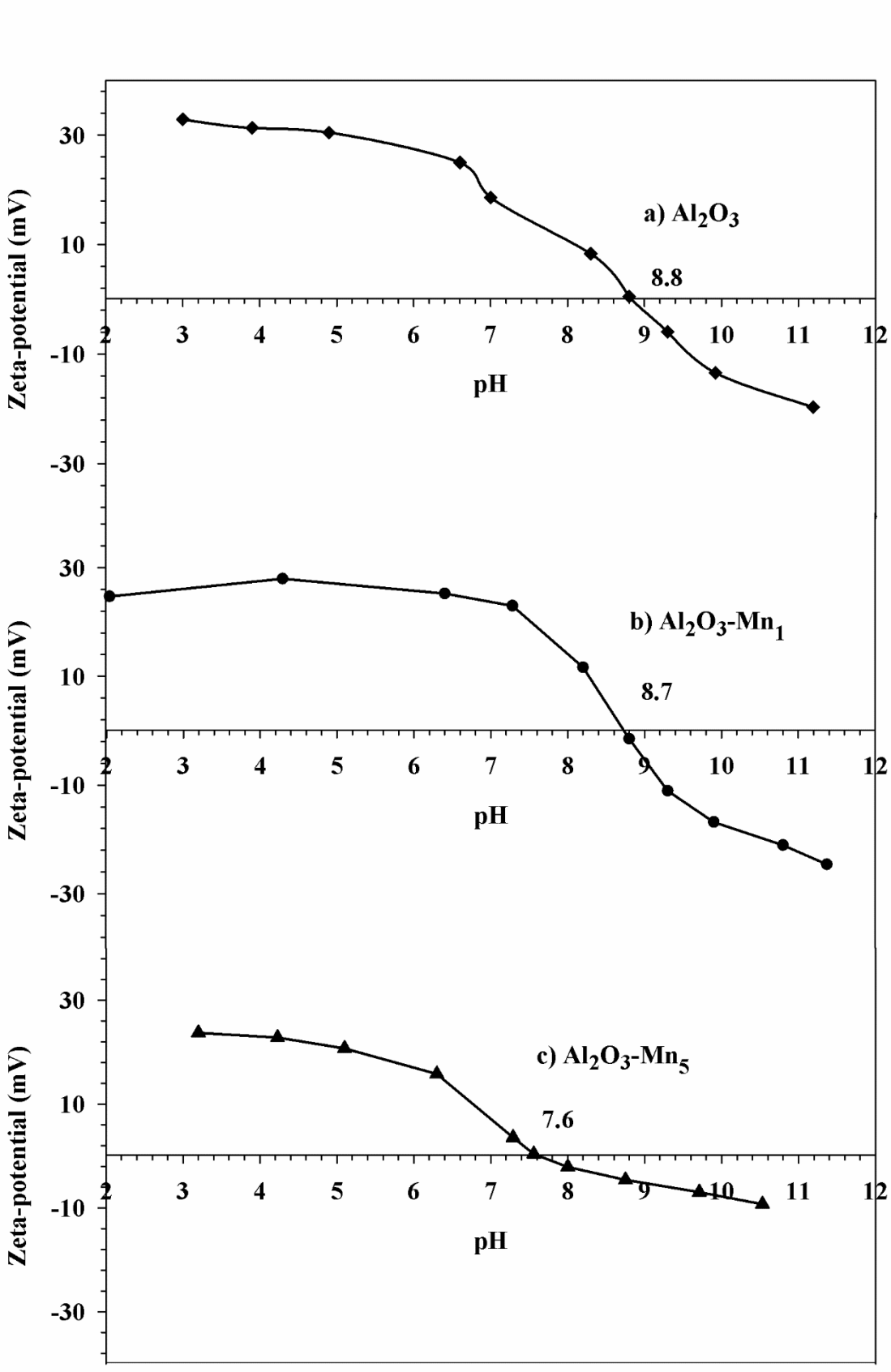

Figure 2. Zeta potential curves of the supports calcined at 500°C: a) Al_2O_3 b) Al_2O_3-Mn_1 and c) Al_2O_3-Mn_5.

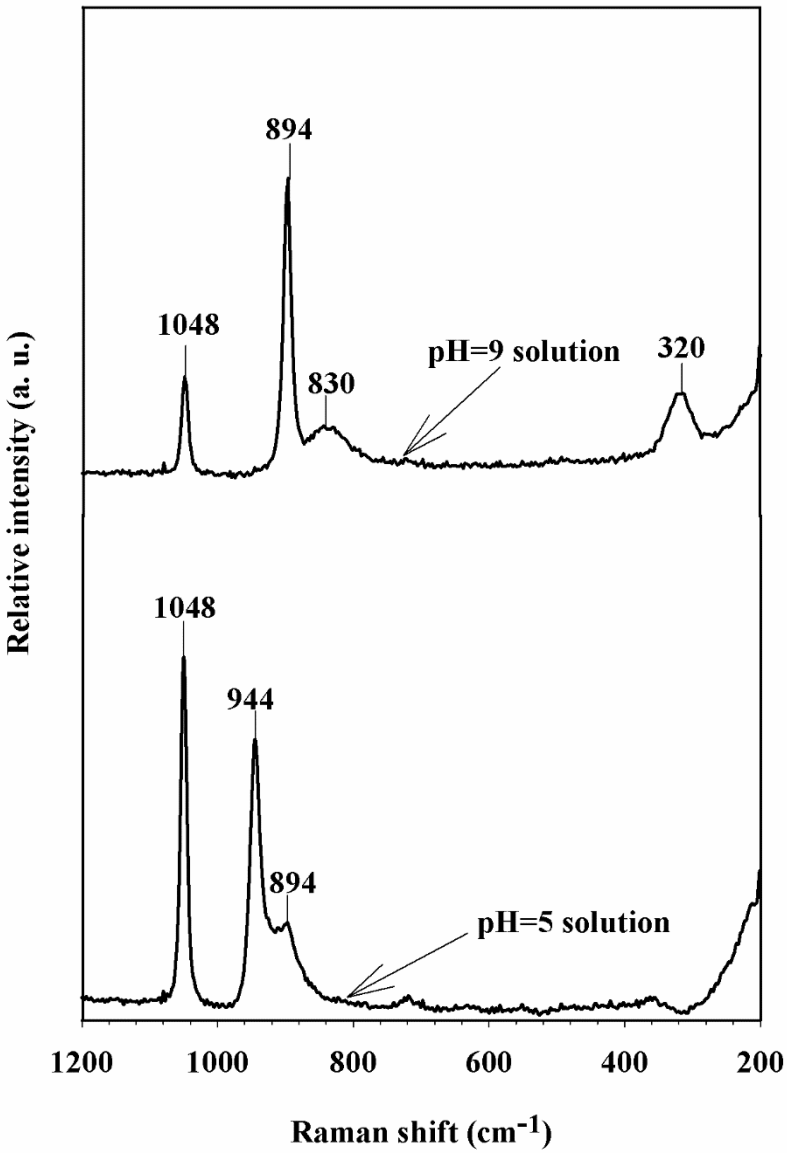

Figure 3. Raman spectra of the impregnation solutions at pH=5 or 9.

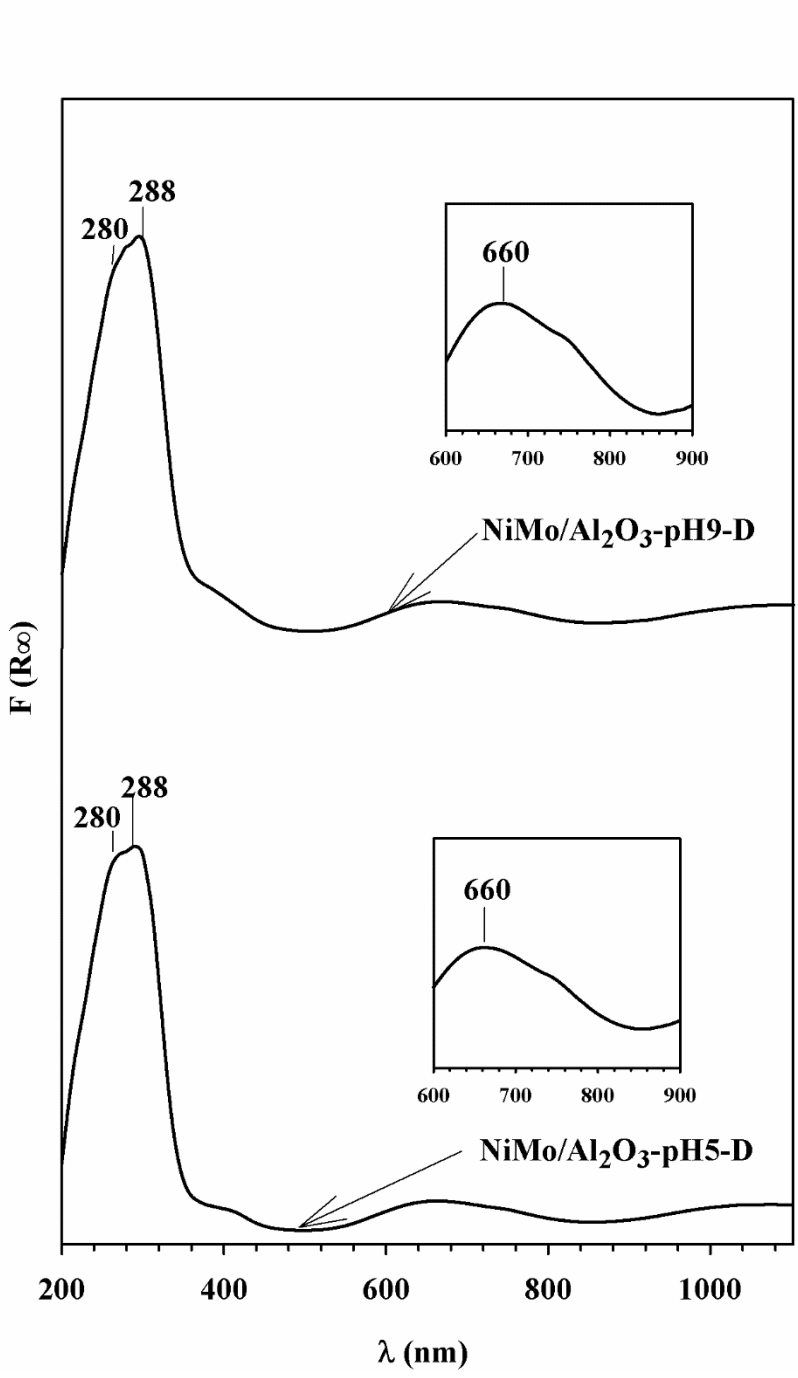

Figure 4. UV-vis diffuse reflectance spectra of dried NiMo/Al_2O_3-pH5-D and NiMo/Al_2O_3-pH9-D.

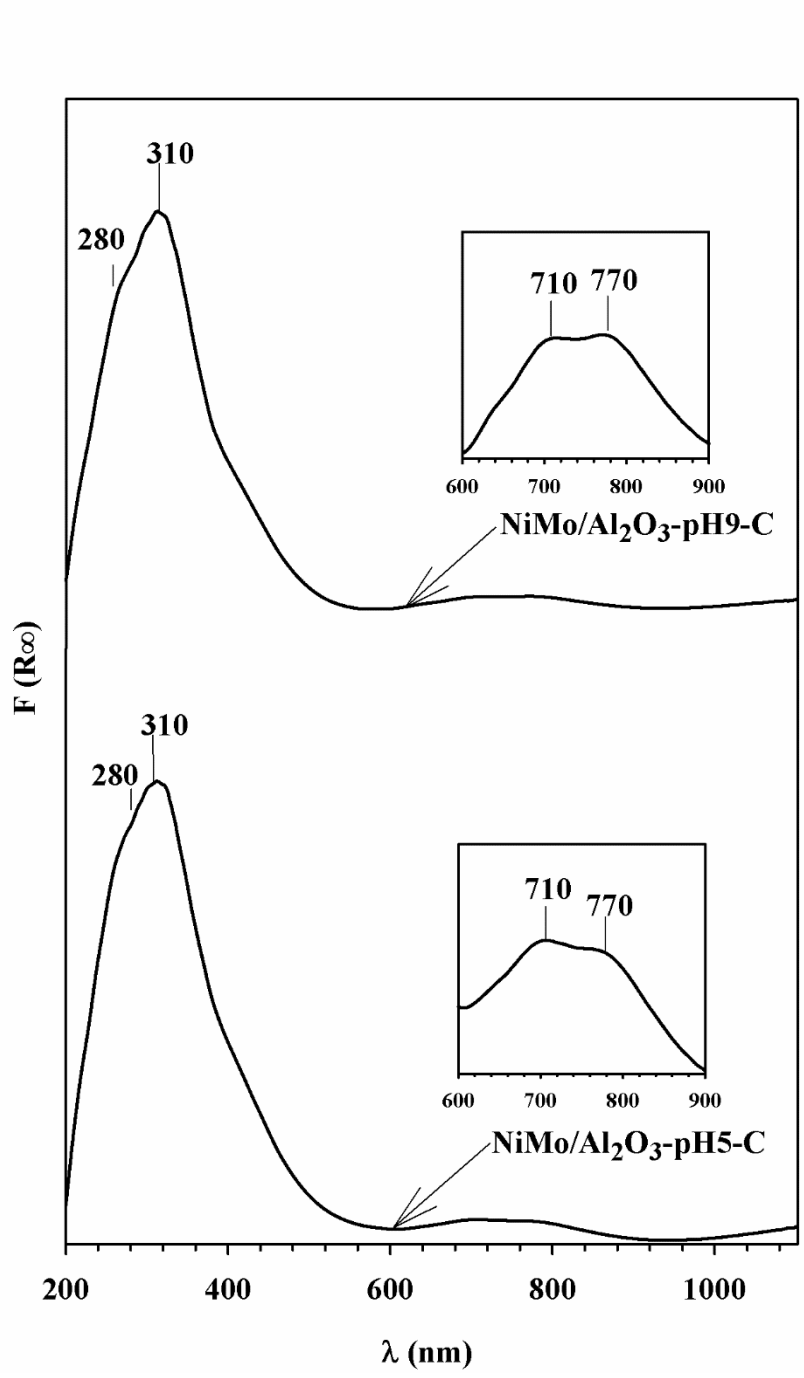

Figure 5. UV-vis diffuse reflectance spectra of calcined NiMo/Al_2O_3-pH5-C and NiMo/Al_2O_3-pH9-C.

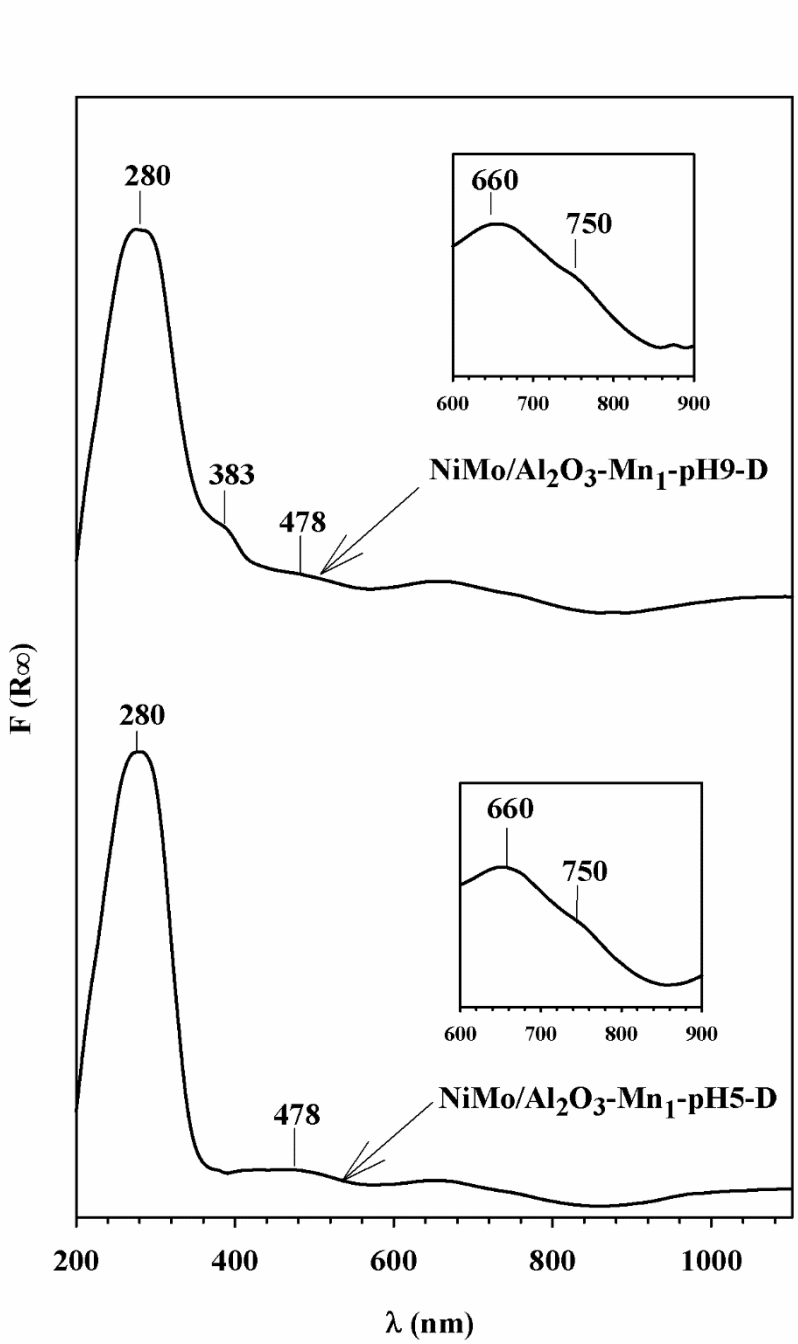

Figure 6. UV-vis diffuse reflectance spectra of the dried NiMo/Al_2O_3-Mn_1-pH5-D and NiMo/Al_2O_3-Mn_1-pH9-D catalysts.

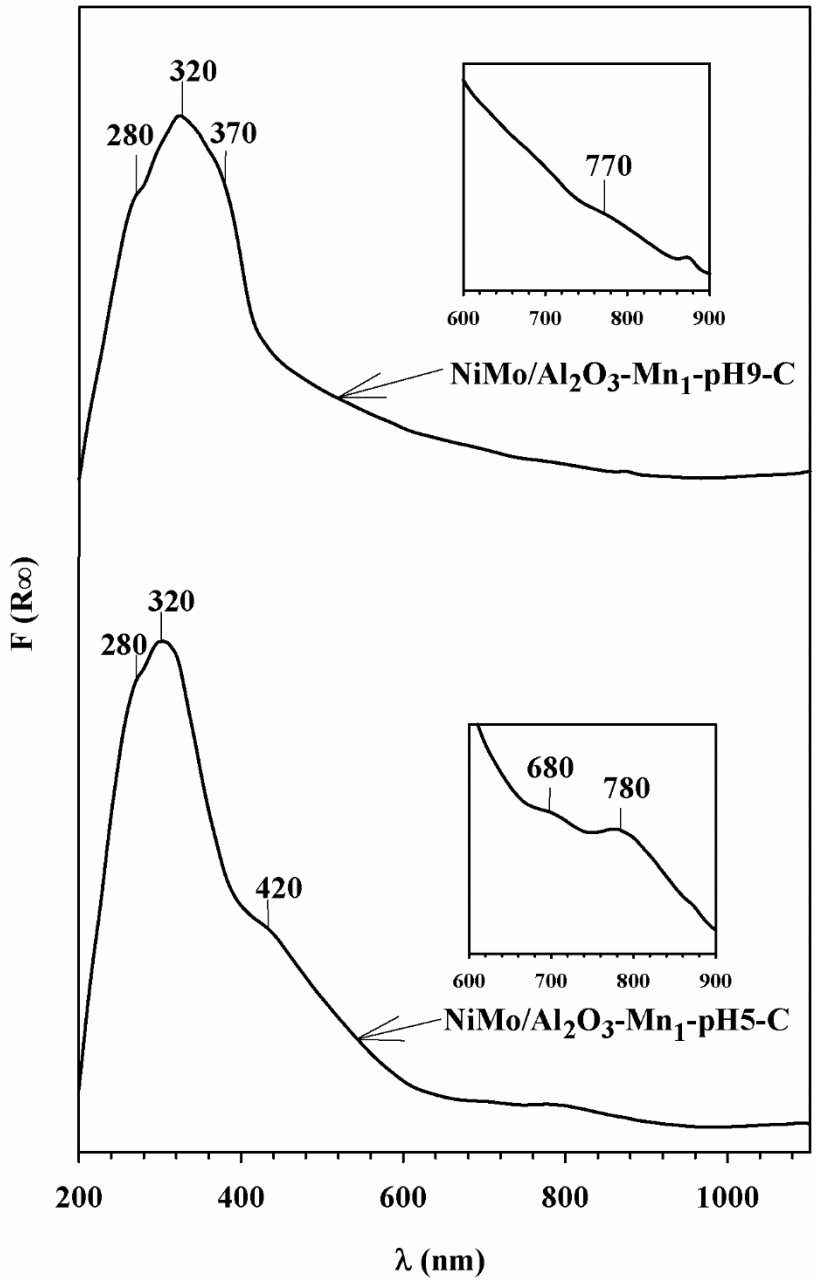

Figure 7. UV-vis diffuse reflectance spectra of the calcined NiMo/Al_2O_3-Mn_1-pH5-C and NiMo/Al_2O_3-Mn_1-pH9-C catalysts.

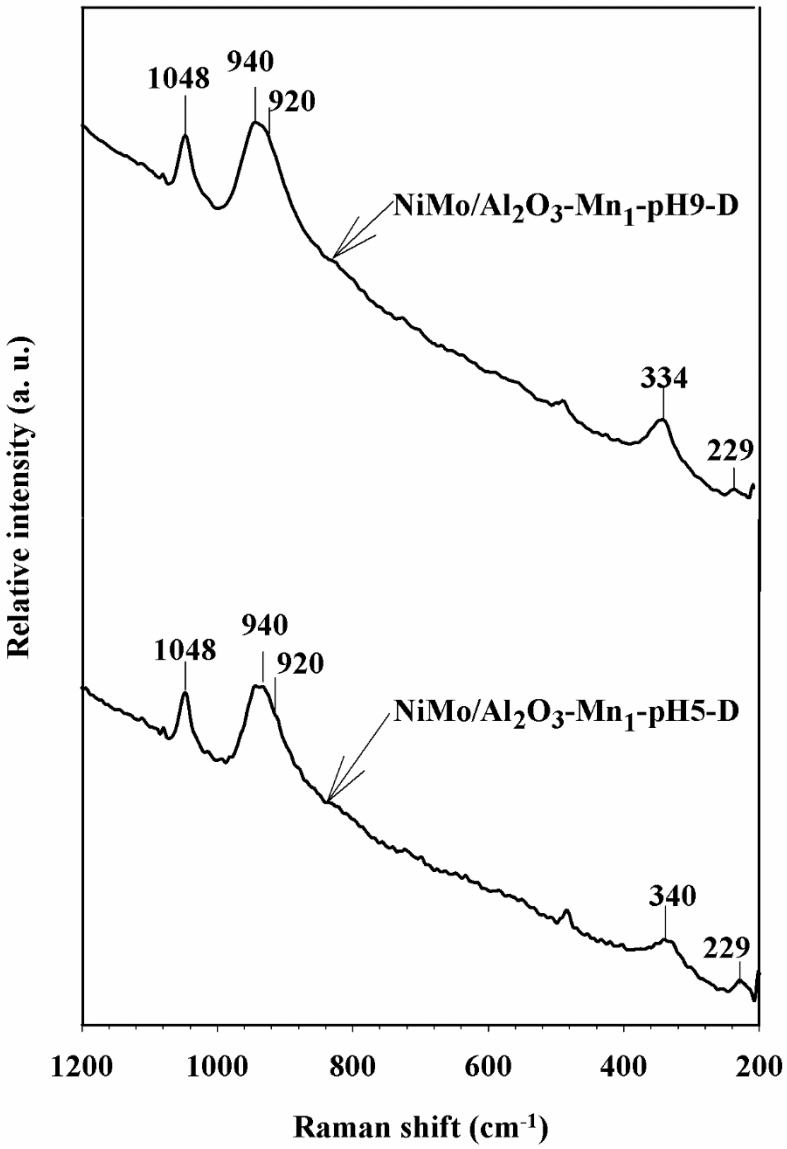

Figure 8. Raman spectra of dried NiMo/Al_2O_3–Mn_1-pH5-D and NiMo/Al_2O_3–Mn_1-pH9-D catalysts.

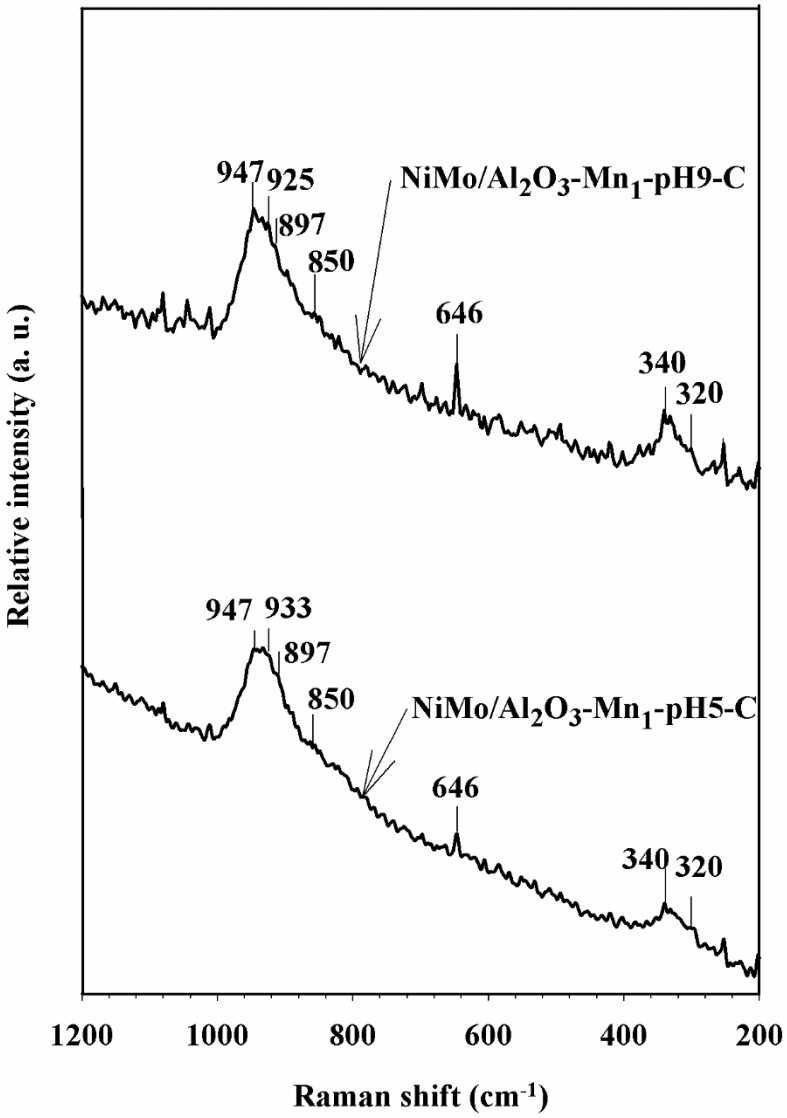

Figure 9. Raman spectra of the calcined NiMo/Al_2O_3–Mn_1-pH5-C and NiMo/Al_2O_3–Mn_1-pH9-C catalysts.

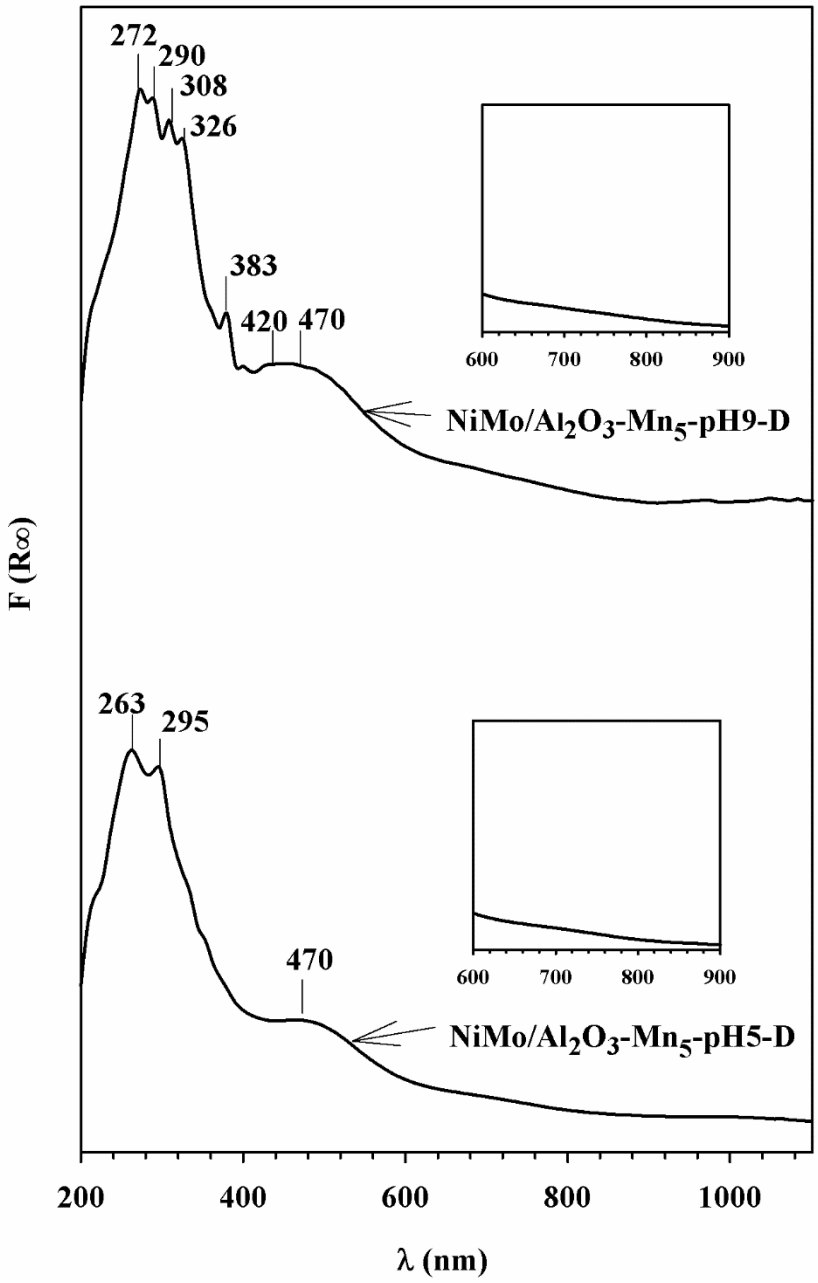

Figure 10. UV-vis diffuse reflectance spectra of the dried NiMo/Al_2O_3–Mn_5-pH5-D and NiMo/Al_2O_3–Mn_5-pH9-D samples.

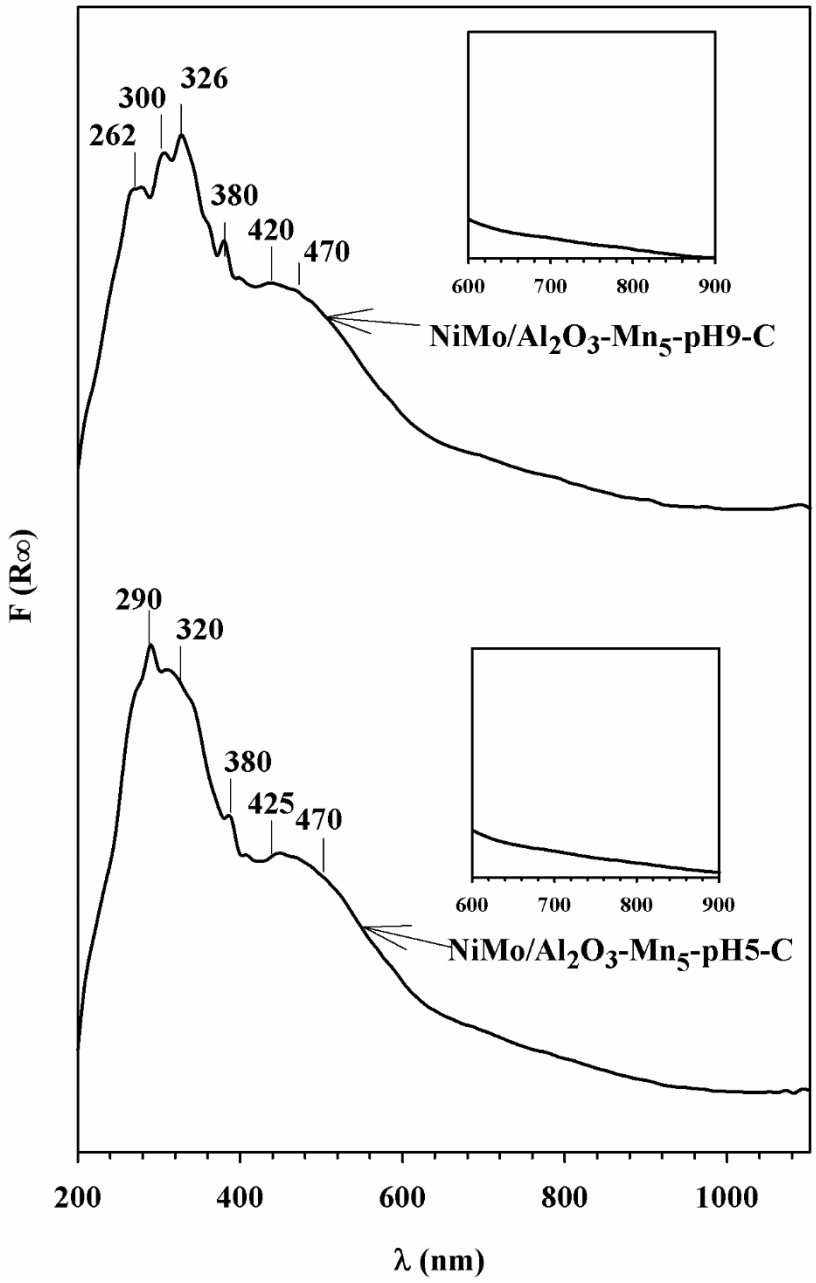

Figure 11. UV-vis diffuse reflectance spectra of the calcined NiMo/Al_2O_3–Mn_5-pH5-C and NiMo/Al_2O_3–Mn_5-pH9-C samples.

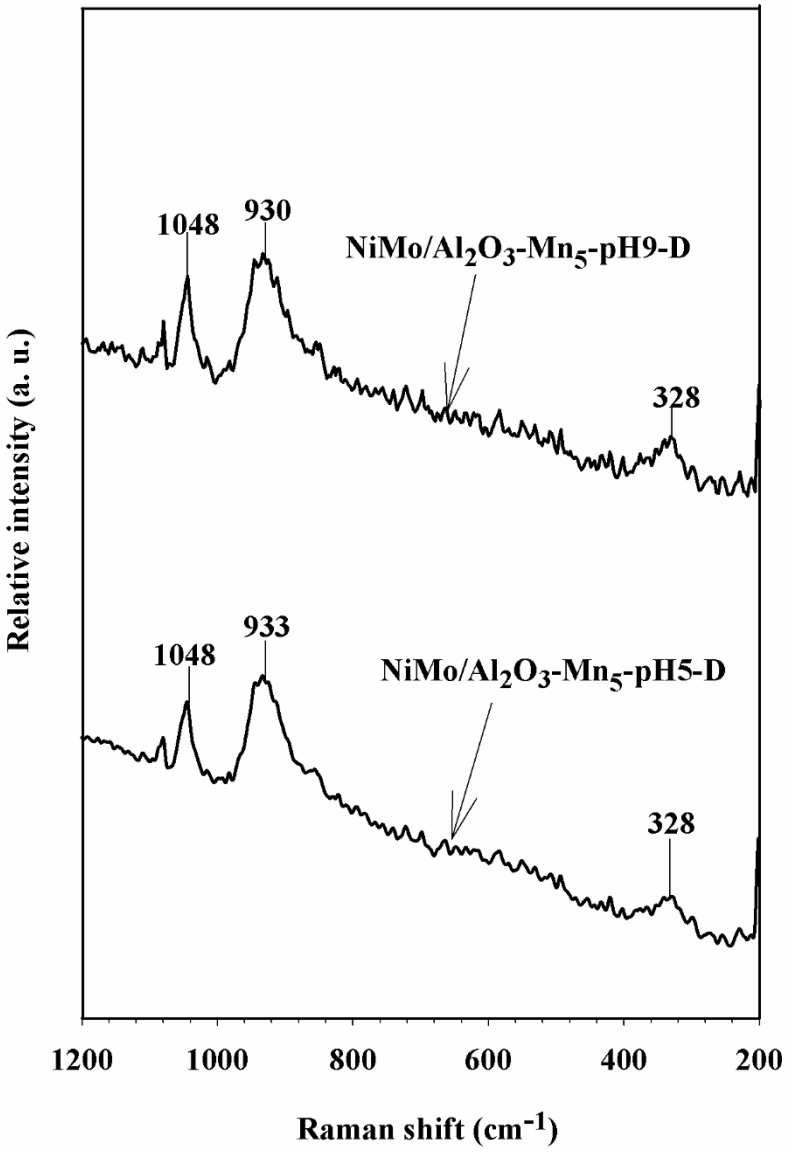

Figure 12. Raman spectra of the dried NiMo/Al_2O_3-Mn_5-pH5-D and NiMo/Al_2O_3-Mn_5-pH9-D catalysts.

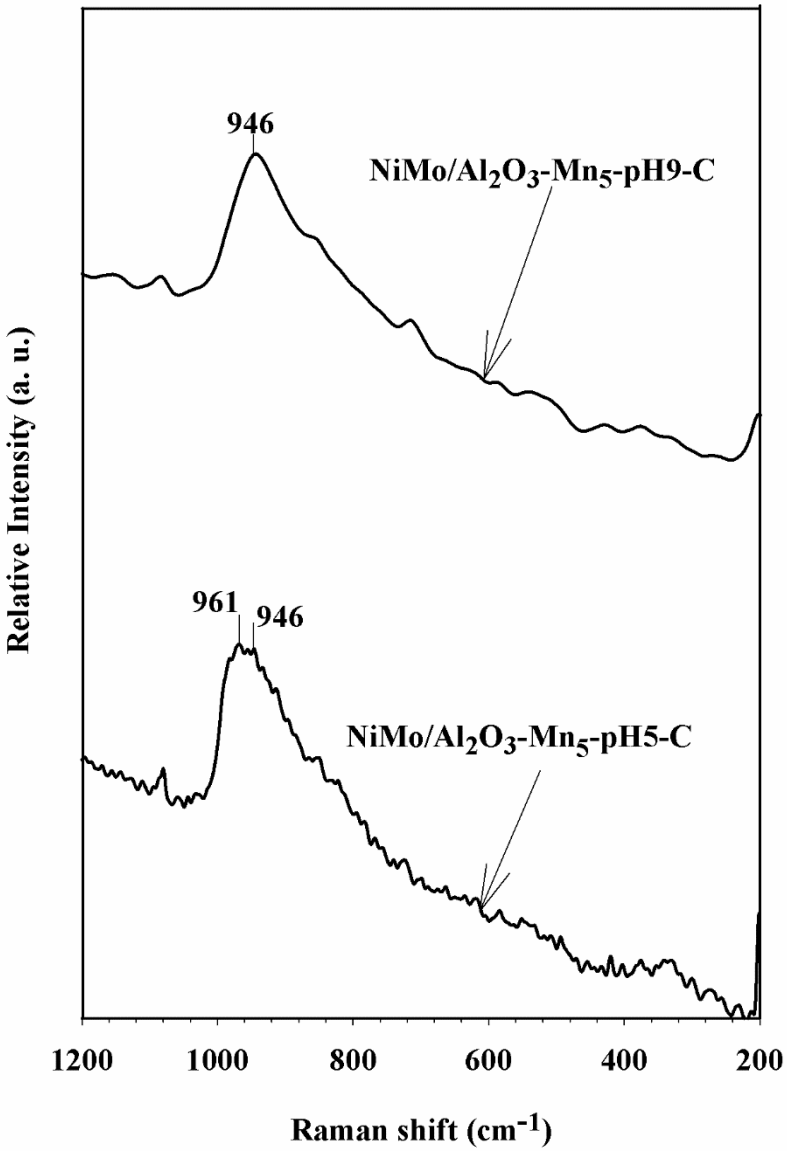

Figure 13. Raman spectra of the calcined NiMo/Al_2O_3-Mn_5-pH5-C and NiMo/Al_2O_3-Mn_5-pH9-C catalysts.

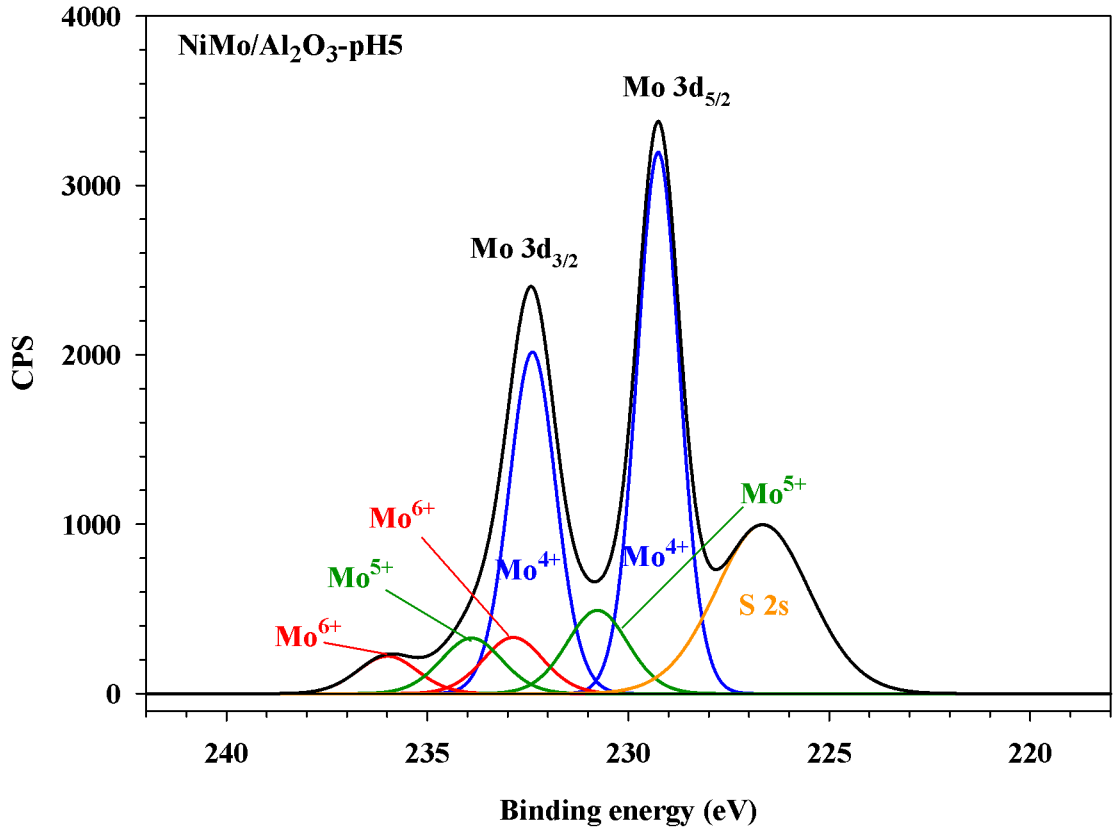

Figure 14. Example of decomposition of Mo 3d XPS core-level spectrum for the NiMo/Al_2O_3-pH5 catalyst sulfided at 400°C for 4 h.

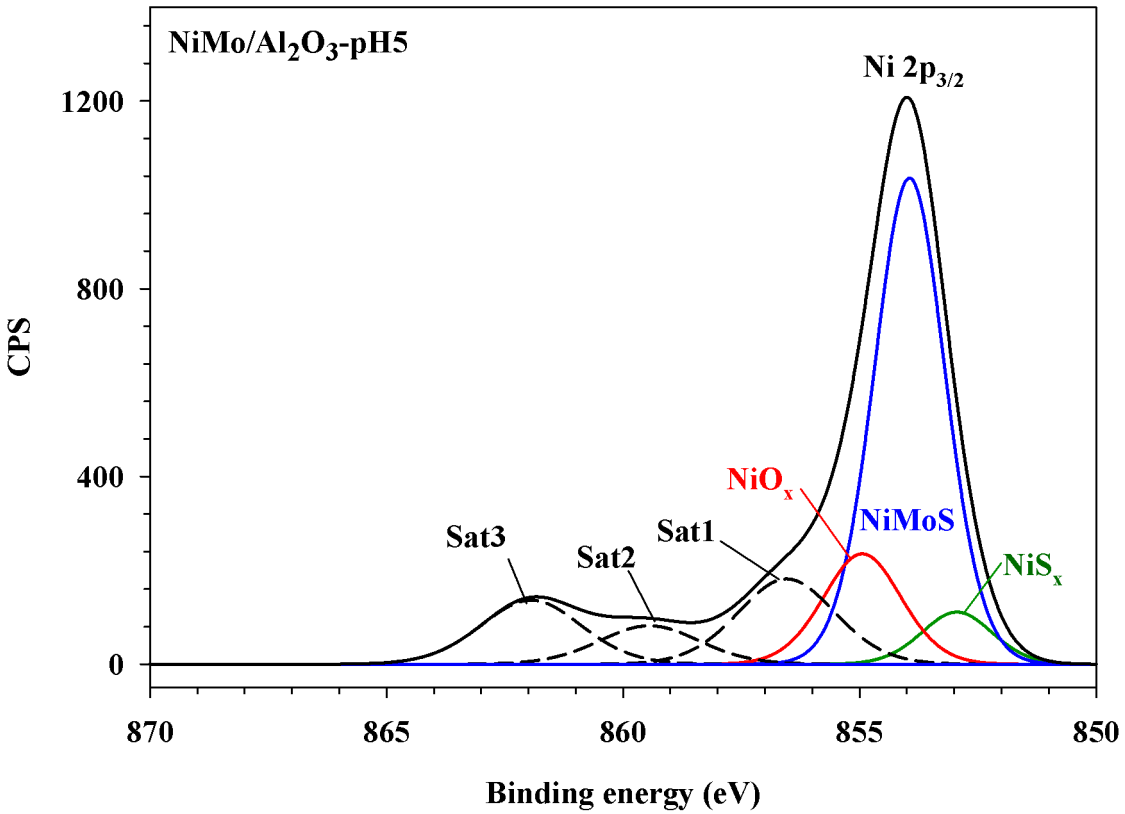

Figure 15. Example of decomposition of Ni $2p_{3/2}$ XPS core-level spectrum for the $NiMo/Al_2O_3$-pH5 catalyst sulfided at 400°C for 4 h.

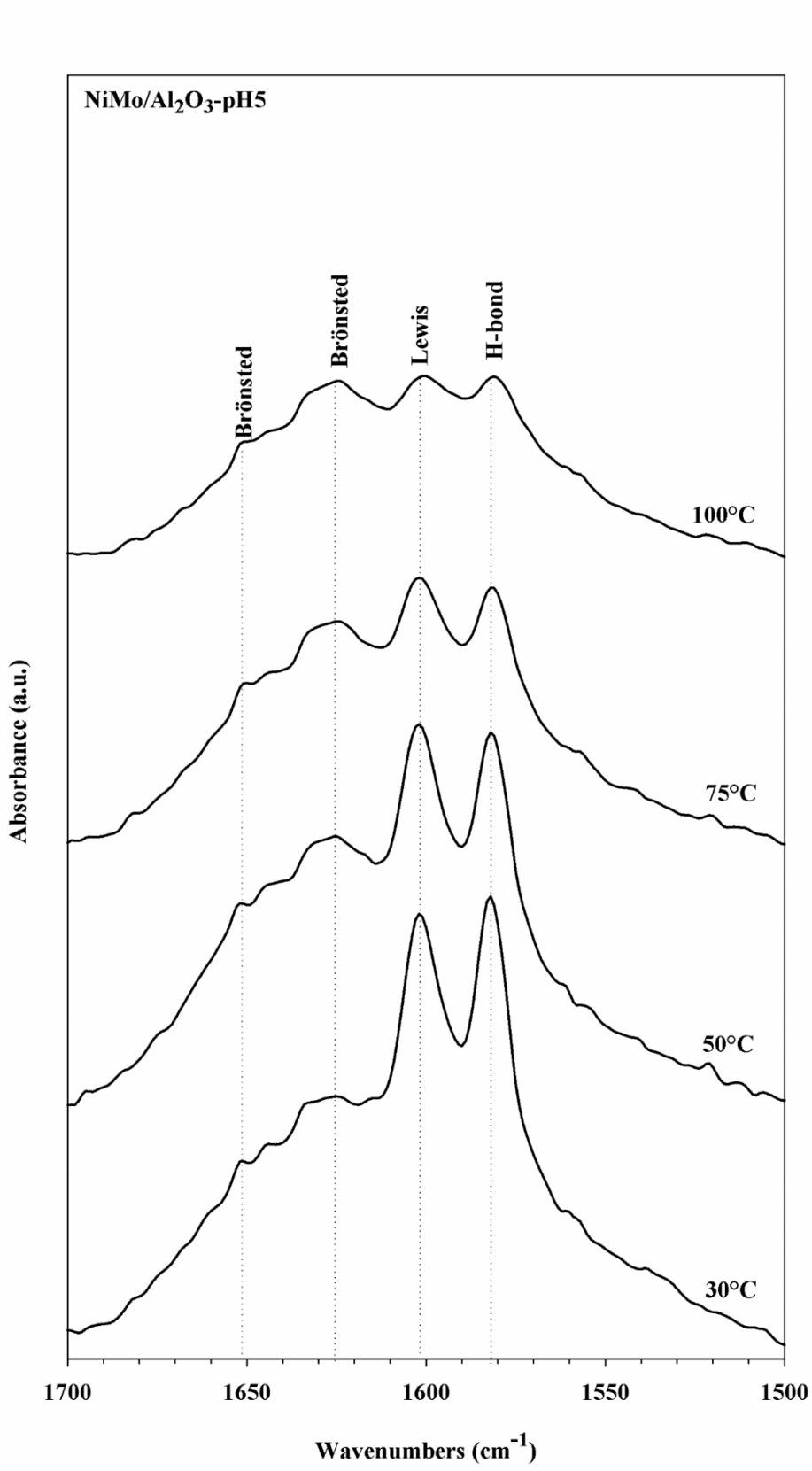

Figure 16. FTIR spectra of lutidine adsorbed on the NiMo/Al_2O_3-pH5 sulfided catalyst for different temperatures of desorption (30, 50, 75 and 100°C).

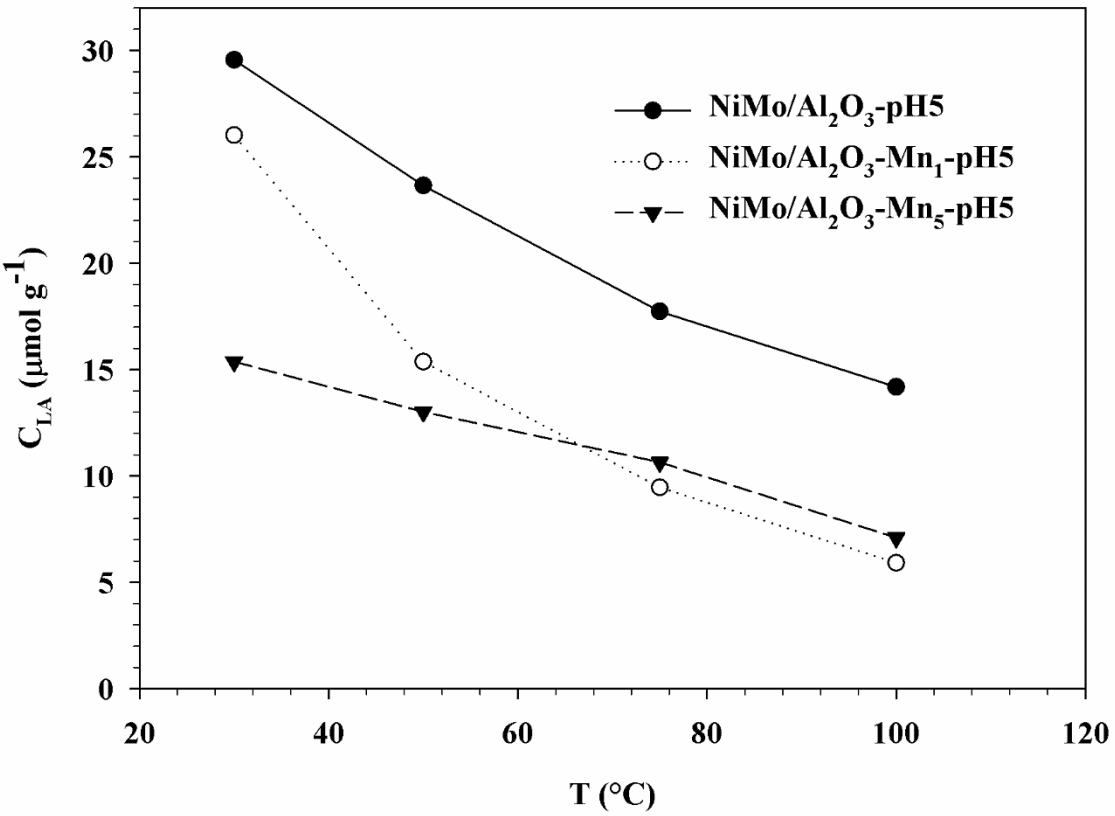

Figure 17. Evolution of the concentration of Lewis acid sites (C_{LA}) in function of the desorption temperature for the NiMo catalysts supported on Al_2O_3, Al_2O_3-Mn_1, Al_2O_3-Mn_5 in the case of an impregnation at pH=5.

Synthesis of NiMo Catalysts supported on Mn-Al_2O_3 for obtaining Green Diesel from Waste Soybean Oil

Supporting Information

I. Vázquez-Garrido[1], A. López-Benítez[1], A. Guevara-Lara[1,*], G. Berhault[2,*]

[1] Área Académica de Química, Universidad Autónoma del Estado de Hidalgo, Carr. Pachuca-Tulancingo Km. 4.5, C.P. 42184 Pachuca, Hidalgo, México.

[2] Institut de Recherches sur la Catalyse et l'Environnement de Lyon, CNRS – Université Lyon I, 02 avenue Albert Einstein, 69100 Villeurbanne, France

All correspondence should be sent to:

Alfredo Guevara-Lara:

Ph: (+52) 7717172000 ext 2202. Fax: (+52) 7717172000 ext 6502

E-mail: guevaraa@uaeh.edu.mx

E-mail: guevaraa@uaeh.edu.mx

Or to :

Gilles Berhault

Ph: (+33) 472 44 53 07

Fax: (+33) 472 44 53 99

E-mail: gilles.berhault@ircelyon.univ-lyon1.fr

Table S1. Selectivity (S_x) in the different hydrocarbons formed by deoxygenation of free fatty acids using the NiMo catalysts supported on Al_2O_3-Mn_1 and on Al_2O_3-Mn_5. Comparison to the NiMo/Al_2O_3 reference catalysts (T = 380° C, P = 40 bars).

		Selectivity (%)				
Catalyst	Oil	C18	C17	C16	C15	S_{HDO}
NiMo/Al_2O_3-pH5	New	12	76	3	9	0.16
	Waste	11	71	2	16	0.16
NiMo/Al_2O_3-pH9	New	13	72	4	11	0.18
	Waste	7	74	2	17	0.10
NiMo/Al_2O_3-Mn_1-pH5	New	9	91	0	9	0.09
	Waste	8	69	3	20	0.12
NiMo/Al_2O_3-Mn_1-pH9	New	16	67	1	16	0.24
	Waste	10	66	8	16	0.15
NiMo/Al_2O_3-Mn_5-pH5	New	8	74	2	16	0.11
	Waste	10	64	14	12	0.16
NiMo/Al_2O_3-Mn_5-pH9	New	14	62	7	17	0.23
	Waste	11	62	4	22	0.17

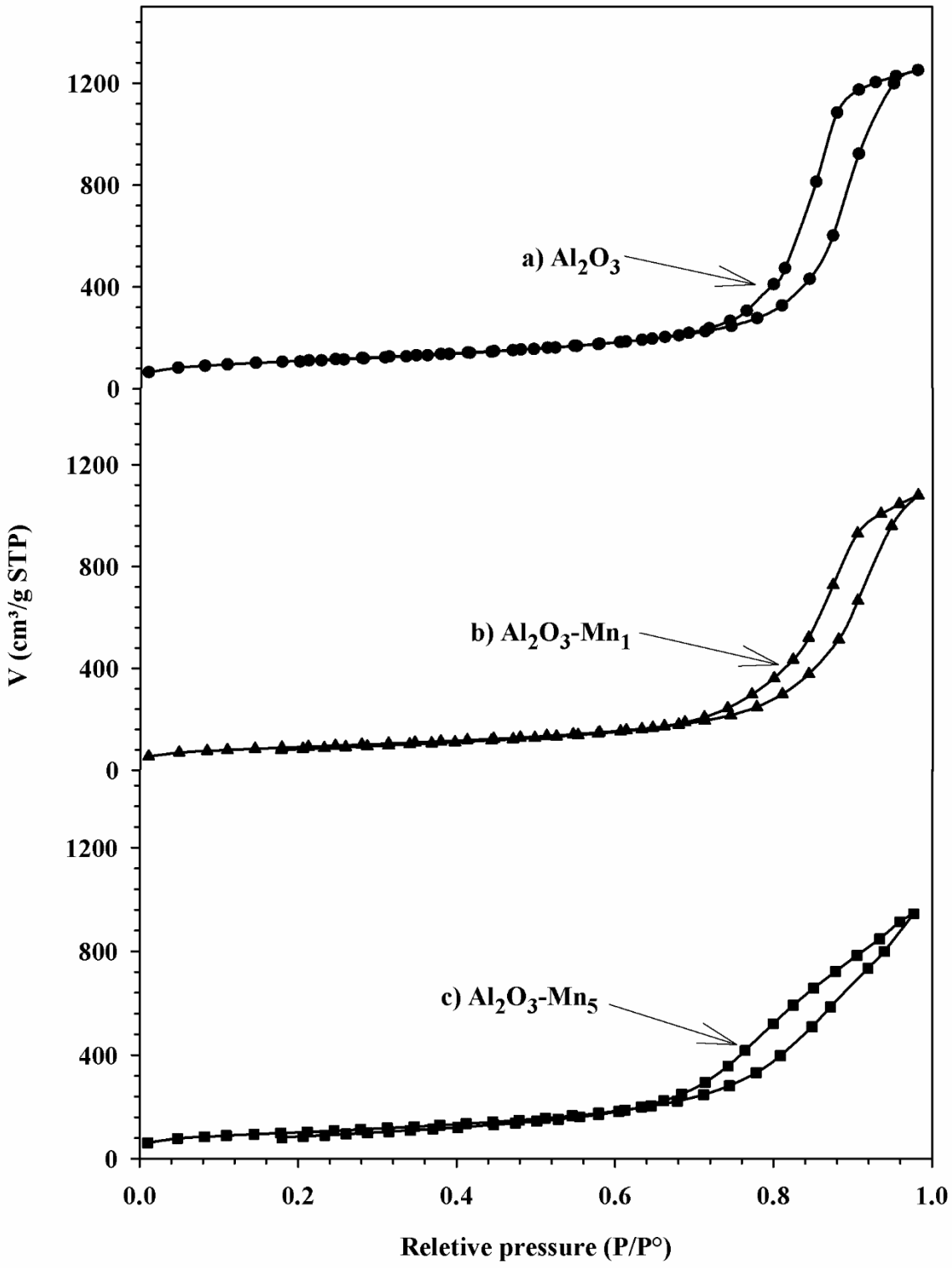

Figure S1. N_2 adsorption-desorption isotherms of the Al_2O_3, Al_2O_3-Mn_1 and Al_2O_3-Mn_5 supports calcined at 500°C.

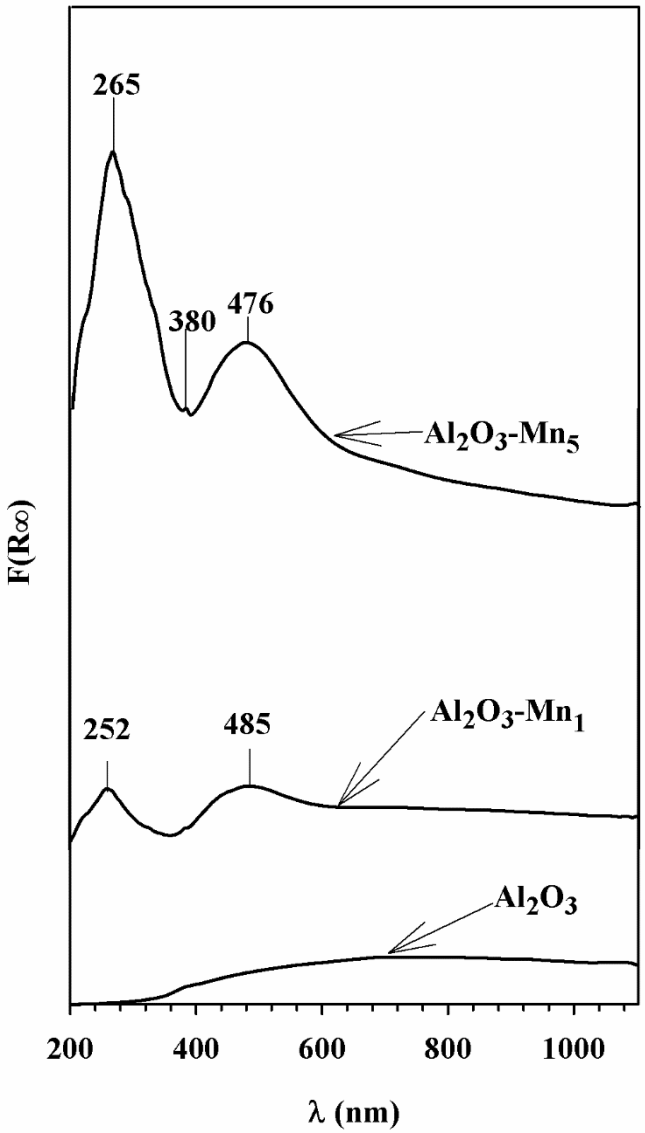

Figure S2. UV-vis DR spectra of the Al_2O_3, Al_2O_3-Mn_1 and Al_2O_3-Mn_5 supports calcined at 500°C.

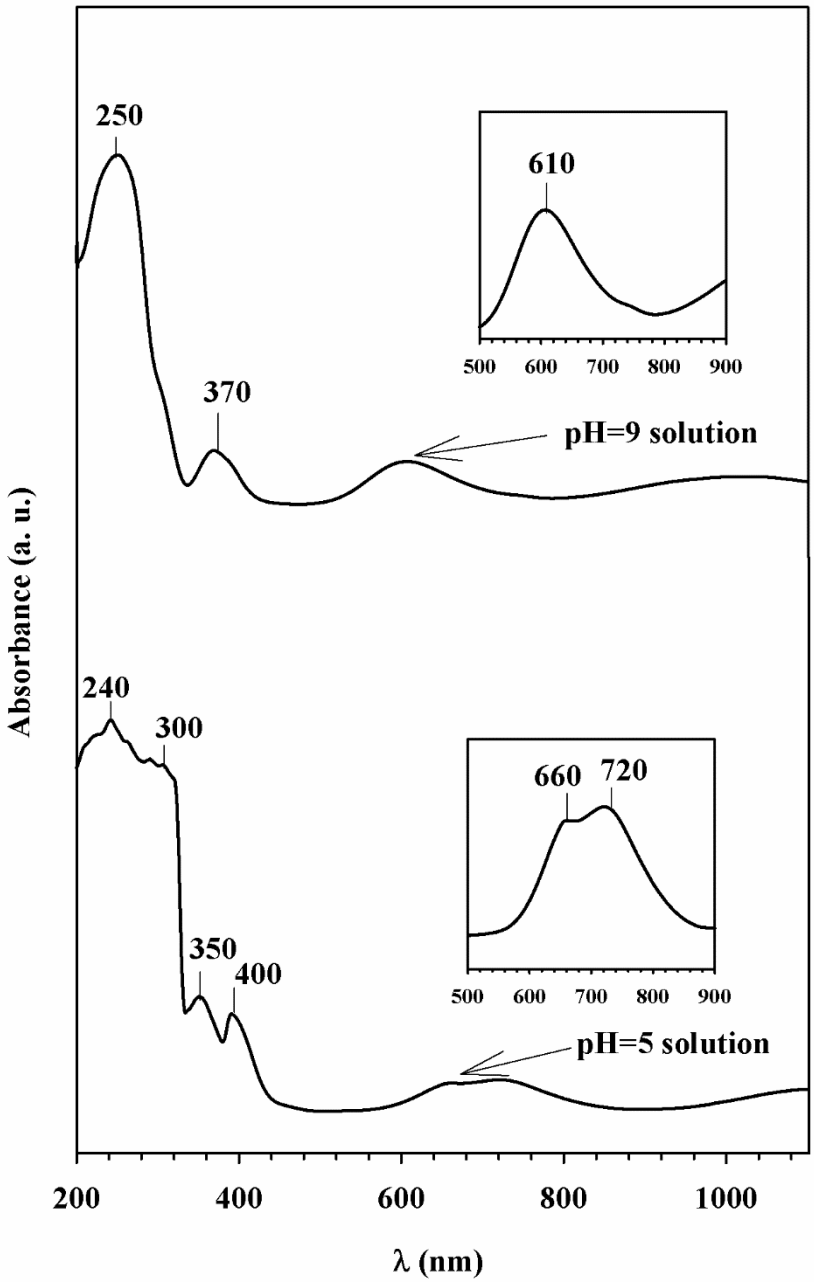

Figure S3. UV-vis spectra of the impregnation solutions at pH=5 or 9.

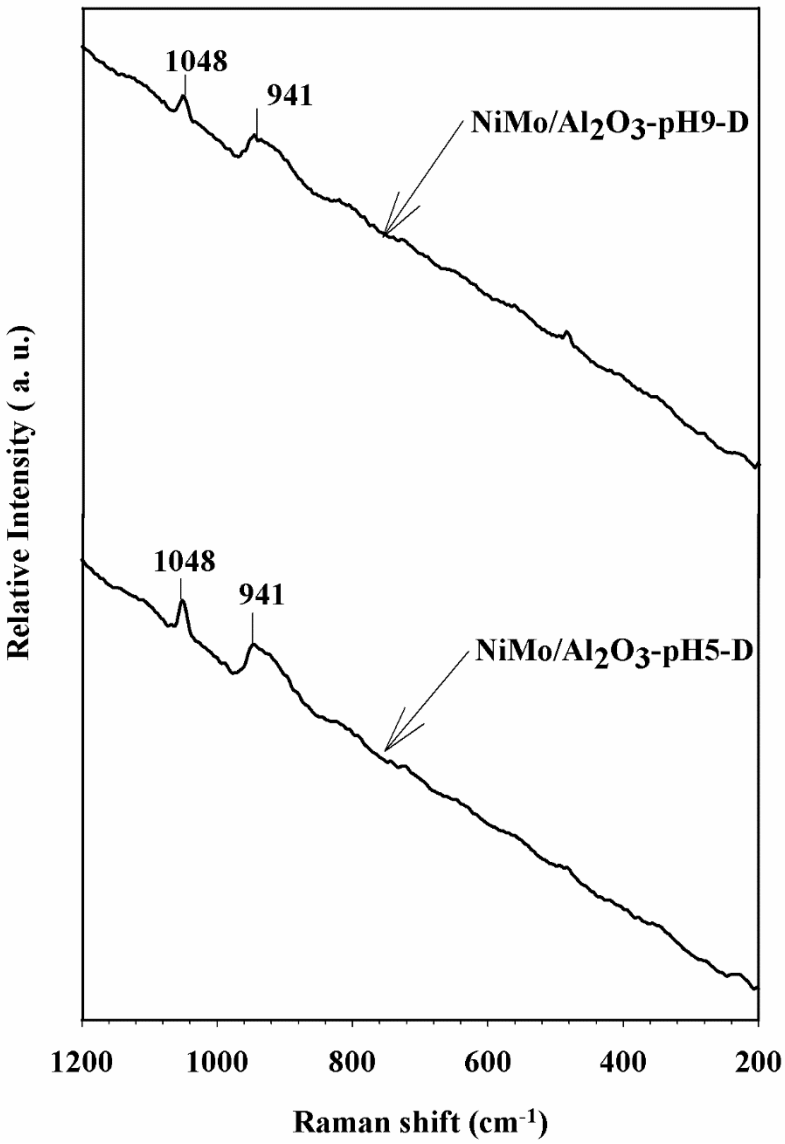

Figure S4. Raman spectra of the dried NiMo/Al_2O_3-pH5-D and NiMo/Al_2O_3-pH9-D catalysts.

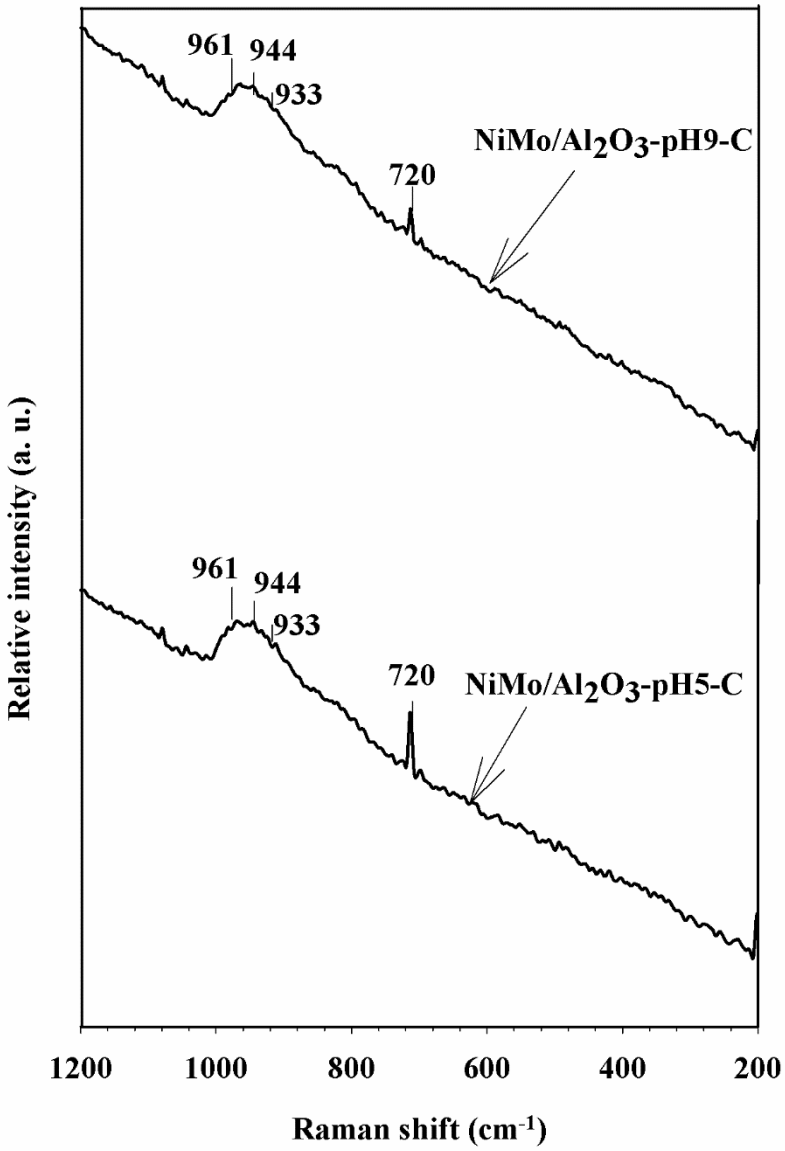

Figure S5. Raman spectra of the calcined NiMo/Al_2O_3-pH5-C and NiMo/Al_2O_3-pH9-C catalysts.

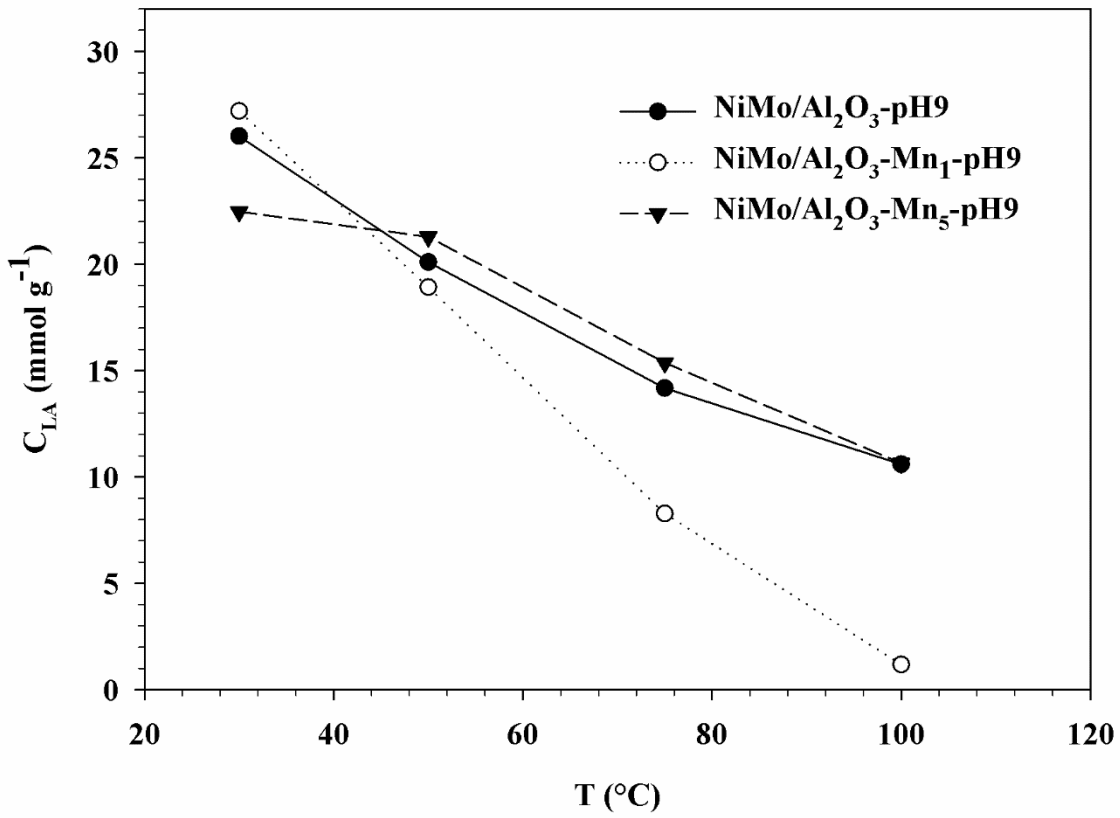

Figure S6. Evolution of the concentration of Lewis acid sites (C_{LA}) in function of the desorption temperature for the NiMo catalysts supported on Al_2O_3, Al_2O_3-Mn_1, Al_2O_3-Mn_5 in the case of an impregnation at pH=9.